

## UC Davis

### UC Davis Previously Published Works

**Title**

The Creston, California, meteorite fall and the origin of L chondrites

**Permalink**

<https://escholarship.org/uc/item/1tj2s85x>

**Journal**

Meteoritics and Planetary Science, 54(4)

**ISSN**

1086-9379

**Authors**

Jenniskens, Peter

Utas, Jason

Yin, Qing-Zhu

et al.

**Publication Date**

2019-04-01

**DOI**

10.1111/maps.13235

Peer reviewed



# Magnetostratigraphy of the Ganyanchi (Salt Lake) Basin along the Haiyuan fault, northeastern Tibet

Shengxue Lei<sup>1,2</sup>, Yanbao Li<sup>1</sup>, Eric Cowgill<sup>3</sup>, Kenneth L. Verosub<sup>3</sup>, Shuaipo Gao<sup>1</sup>, Liangxin Xu<sup>1</sup>, and Yongkang Ran<sup>4,1</sup>

<sup>1</sup>Key Laboratory of Active Tectonics and Volcanos, Institute of Geology, China Earthquake Administration (CEA), Beijing 100029, China

<sup>2</sup>Tianjin Earthquake Bureau, Tianjin 300201, China

<sup>3</sup>Department of Earth and Planetary Sciences, University of California, Davis, California 95616, USA

<sup>4</sup>State Key Laboratory of Earthquake Dynamics, Institute of Geology, China Earthquake Administration (CEA), Beijing 100029, China

## ABSTRACT

Although Quaternary deposits within the Ganyanchi (Salt Lake) pull-apart basin along the eastern Haiyuan fault preserve a record of both the paleo-environmental and tectonic evolution of the northeastern Tibetan Plateau, this sedimentary archive has yet to be dated. Here we report a paleomagnetic study of a 328-m-long sediment core drilled near the modern depocenter of the basin, and use this record to both date the onset of sedimentation and reconstruct the depositional history of the basin. The observed magnetic polarity sequence comprises 13 normal and 12 reversed polarity zones, and we explore two possible correlations to the geomagnetic polarity time scale. Our preferred correlation minimizes changes in sedimentation rate and extends from the Brunhes normal polarity chron to the Gauss normal polarity chron. This correlation indicates that the Ganyanchi Basin began to develop by at least ca. 2.76 ± 0.03 Ma. Sediment accumulation rates (SAR) were elevated in two intervals, from ca. 1.92 to 1.78 Ma, when they were ~130.3 m/m.y., and from ca. 0.77 Ma to present, when they were ~234.6 m/m.y. We attribute these enhanced depositional episodes to both Northern Hemisphere cooling and local tectonic effects, with SAR values increasing as the regional climate has shifted toward overall drier and cooler conditions.

## INTRODUCTION

Studies of the history of deformation of the Tibetan Plateau indicate that it has grown northward during the Cenozoic Indo-Eurasian collision (e.g., Tapponnier et al., 2001; Pares et al., 2003; Clark et al., 2010), with the most recent deformation and surface uplift occurring in the northeastern part of the plateau (e.g., Tapponnier et al., 2001). Growth of northeastern Tibet appears to have played a key role in the evolution of the East Asian monsoon and Asian aridification (e.g., An et al., 2001; Guo et al., 2002; Pares et al., 2003; Dupont-Nivet et al., 2007; Zheng et al., 2010; Zhang et al., 2012). However, the paucity of precise ages for basin sediments within the plateau handicaps understanding of both the tectonic evolution of northeastern Tibet and paleoenvironmental change in the region.

The Ganyanchi (Salt Lake) pull-apart basin is located along the eastern part of the active, left-lateral Haiyuan strike-slip fault in northeastern Tibet (Fig. 1). Such pull-apart basins host sediments that contain abundant information regarding the deformational history of the bounding strike-slip fault (Mann et al., 1983; Ding et al., 2004). Moreover, the high rates of deposition and thick accumulations of sediment within pull-apart basins (Basile and Brun, 1999) can also preserve important paleoenvironmental records. Due to its location in northeastern Tibet, the Ganyanchi Basin preserves an important sedimentary record of tectonism and climate change associated with progressive growth of the Tibetan Plateau (Zhang et al., 1991; Burchfiel et al., 1991).

In order to study the history of sediment accumulation in the Ganyanchi pull-apart basin, a drilling program was carried out near the depocenter of the basin in 2014–2015, which yielded a continuous long (~328 m) core mainly consisting of fluvio-lacustrine sediments. The present study uses high-resolution paleomagnetic results from this core to date both the core and the onset of deposition, as well as reconstruct the depositional history of the basin. These magnetostratigraphic data provide a basic age framework for this region that is intended to serve as a starting point for future studies on climate and sedimentation patterns in northeastern Tibet. There are few core records of the age range covered here from basins in this region, and none to our knowledge from basins along the Haiyuan fault. Thus, the present investigation provides a useful sedimentary record of the climatic and tectonic history of northeastern Tibet. Here we find that sediment accumulation rate (SAR) values increased as the regional climate shifted toward overall drier and cooler conditions.

## GEOLOGIC SETTING

The Haiyuan fault is a ~1000-km-long active sinistral strike-slip fault (Fig. 1) that connects the tectonically active Qilian Shan to the west with the seismically active Liupan Shan in the east (Zhang et al., 1991; Li et al., 2009) (Fig. 1). Based on differences in geometry and seismicity, the fault can be divided near the Yellow River (Huang He; ~34°N, 104°E) into western and eastern sections. The eastern Haiyuan fault is punctuated by eight pull-apart basins that range in strike-perpendicular width from 1 to 3 km and strike-parallel length from 2

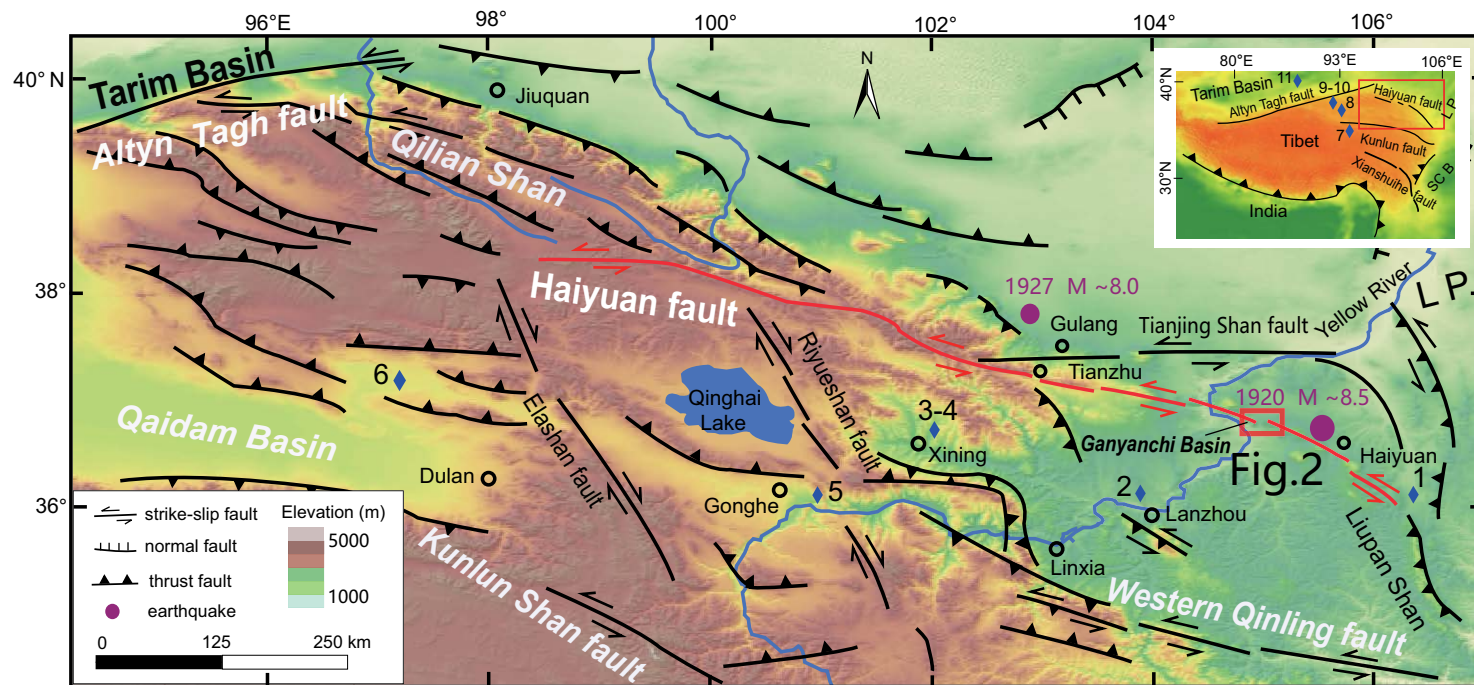
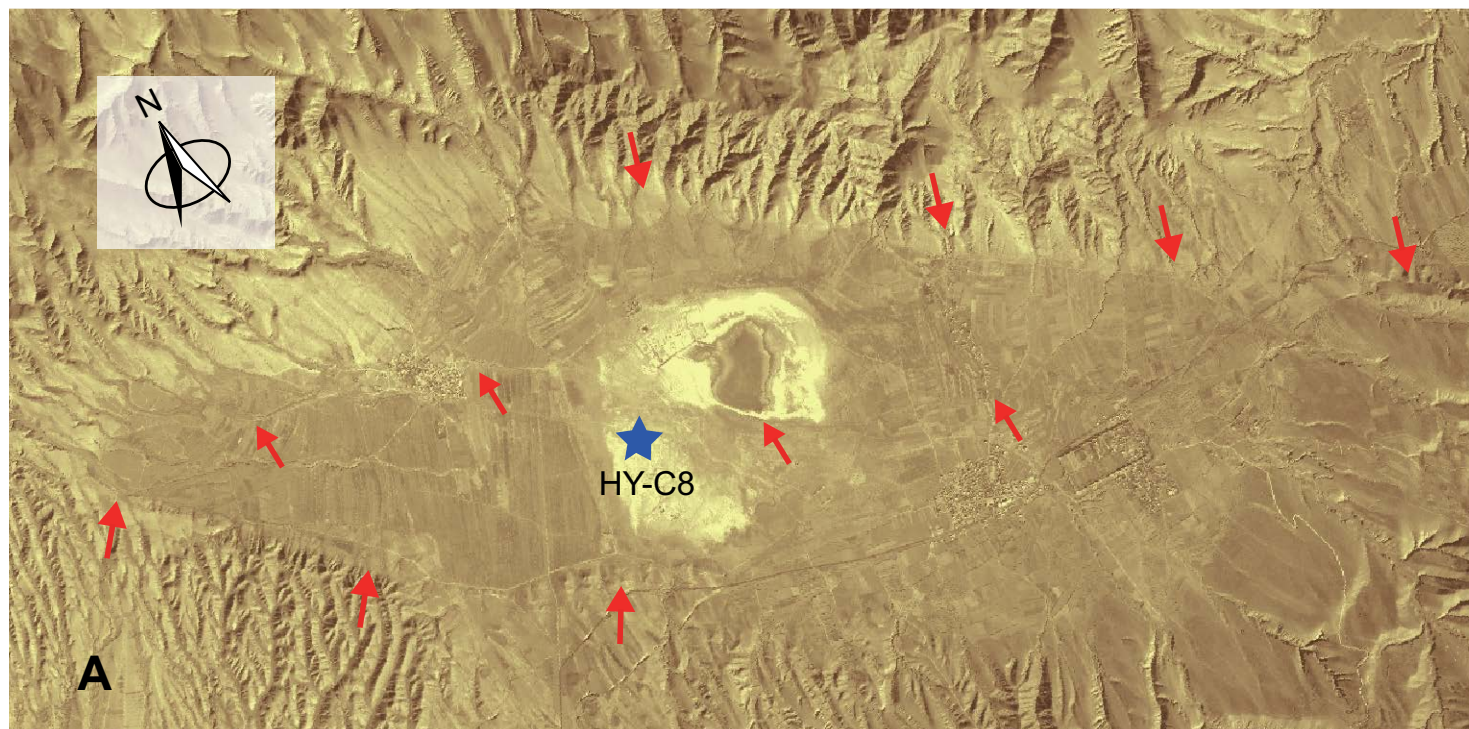


Figure 1. Map of the northeastern Tibetan Plateau showing the location of the Ganyanchi Basin in the context of the Haiyuan fault (red line) and other major structures (modified from Yuan et al., 2013). Red box indicates the location of Figure 2; inset shows the Tibetan Plateau (LP—Chinese Loess Plateau; SCB—Sichuan Basin, the approximate elevations of the orange and dark-green are >4000 m and <500 m, respectively). Blue diamonds on the main map and inset show select sites where sediment accumulation rates (SARs) have been determined magnetostratigraphically across the northeastern Tibetan Plateau: 1—Sikouzi Basin (Wang et al., 2011); 2—Lanzhou (Zhang et al., 2016); 3, 4—Xining (Lu et al., 2012); 5—Guide Basin (Fang et al., 2005); 6—eastern Qaidam Basin (Fang et al., 2007); 7—Kunlun Shan Pass Basin (Song et al., 2005); 8, 9, 10—western Qaidam Basin (Chen et al., 2017; Zhang et al., 2012; Zhang et al., 2014); 11—eastern Tarim Basin (Chang et al., 2012). See Table 4 for a compilation of SAR values. Purple dots indicate epicenters of select major 20<sup>th</sup>-century earthquakes, labeled with year and magnitude. F—fault.

to 8 km (Deng et al., 1984). The Ganyanchi Basin has a regular rhomboidal shape and is the largest of these basins, with an along-strike length of ~8 km and a cross-fault width of ~3 km (Deng et al., 1989). The width-to-length ratio of 2.7 is similar to the global average value (~3), which is scale independent (Aydin and Nur, 1982). The eastern Haiyuan fault was the locus of the *M* ~8.5 Haiyuan earthquake (Deng et al., 1984), which struck the Haiyuan County area on 16 December 1920.

The Ganyanchi Basin is located at a left-stepping, releasing step-over in the central part of the eastern Haiyuan fault (Fig. 2B) and ~3 km west of the epicenter for the 1920 event (ISL and SBNHAG, 1980; Deng et al., 1989). The northeastern margin of the basin is defined by the Nanhuashan-Xihuashan fault (F1 on Fig. 2B) and the Huangjiawa range to the northeast. The south-western margin of the basin is defined by the Huangjiawa Shan fault (F2 on Fig. 2B) and Xihua range. Topographic relief between the basin and crests of the flanking ranges is ~300–500 m. The basin-bounding faults cut Quater-

nary deposits and locally have a normal component of slip (e.g., Burchfiel et al., 1991), with topographic ridges in the adjacent mountain ranges terminating in triangular facets at the faults (Fig. 2A). The basin interior is cut by the Ganyanchi-Shaojiazhuang cross-basin fault (F3 on Fig. 2B), which appears to link the two basin-bounding faults (Deng et al., 1989). An active depocenter lies north of the cross-basin fault and hosts a salt lake (Fig. 2). Depth to basement is ~750 m and ~500 m to the north and south of the cross-basin fault, respectively, as indicated by seismic reflection and core data to be reported in our companion study. Within the basin, the ground surface is relatively flat and covered by Holocene alluvial and evaporite deposits (IGCEA and SBNHAG, 1990; Li et al., 2014). The cross-basin fault is expressed as a 1–2-m-high topographic scarp that faces northeast in the basin center (Fig. 2B) and shows paleoseismic evidence of surface rupture in 1920 as well as from several older events (Liu-Zheng et al., 2015; Li et al., 2014). A number of coseismic structures were produced within the basin during the 1920 rupture,



**Figure 2** (on this and following page). Maps of the Ganyanchi pull-apart basin, with the blue star showing the HY-C8 borehole location. (A) Satellite image from the China Centre for Resources Satellite Data and Application (CRESDA); red arrows indicate fault traces. See Figure 1 for location.

including new scarps ~1.5–3 m high along the cross-basin fault in the center of the basin, grabens and horsts with lengths of a few tens of meters or less along 400–500-m-wide zone in Shaojiashuang village, and 3.5–7.5 m offsets of farming fences and terraces in the northeastern part of the basin (ISL and SBNHAG, 1980; IGCEA and SBNHAG, 1990).

The ranges surrounding the Ganyanchi Basin are dominantly underlain by late Proterozoic metamorphic and Cenozoic sedimentary rocks (Fig. 2B) (NBGMR, 1989). Almost no Paleozoic or Mesozoic strata exist in this region, with the exception of rare Devonian purple sandstone exposed along the southwestern edge of the basin (NBGMR, 1989). The late Proterozoic rocks are mainly bluish-gray schist (unit AnЄs) and gray marble (unit AnЄm), with minor gneiss and quartzite (NBGMR, 1989). Cenozoic strata mainly comprise red mudstone and siltstone with numerous gypsum horizons of the Qingshuiying Formation (unit E<sub>3</sub>q), which is of Oligocene age based on ostracod fossils (NBGMR, 1989), together with Quaternary yellowish to brown loess that is extensively exposed in the Haiyuan area (IGCEA and SBNHAG, 1990). In the southwestern part of the basin, layers of dark-gray conglomerate are exposed

south of the Huangjiawa Shan fault, and are assigned to the early Pleistocene by regional lithostratigraphic correlation (IGCEA and SBNHAG, 1990).

With the exception of regional structural mapping (Burchfiel et al., 1991) and paleoseismic studies (Li et al., 2014; Liu-Zheng et al., 2015), no sedimentologic or chronological work has been done in the Ganyanchi pull-apart basin. To address this problem, we drilled a 328-m-long borehole, named HY-C8, south of the cross-basin fault and near the active depocenter (Figs. 2, 3A), and use magnetostratigraphic analyses to constrain the age of the basin and fill. Because the borehole penetrated basement, we are able to characterize the complete sedimentary sequence within the sampled part of the basin.

## METHODS

The diameter of the borehole was 110 mm from the surface to a depth of 200 m, below which it was decreased to 90 mm to reduce the load on the drilling machine. Uniformly oriented core fragments were typically 2–4 m long;

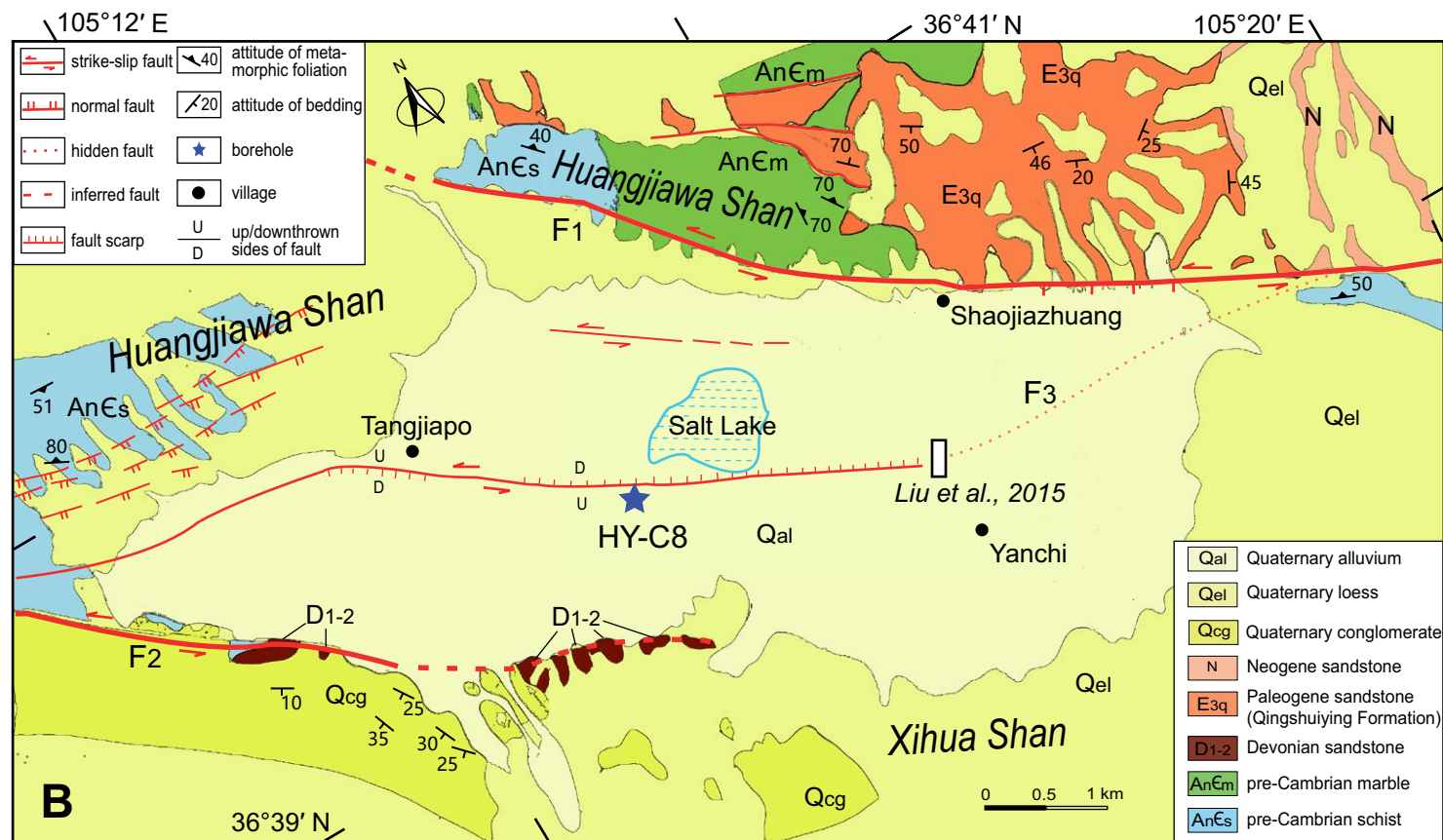


Figure 2 (continued). (B) Simplified geologic map of the same area as in A (modified from Deng et al., 1989). White box indicates the location of a paleoseismic study by Liu-Zheng et al. (2015). Main faults are labeled F1 (Nanhuashan-Xihuashan fault), F2 (Huangjiawa Shan fault) and F3 (Ganyanchi-Shaojiazhuang cross-basin fault).

Supplementary Table S1: Inclination and Polarity Results for Whole Core from Alternating Field and Thermal Demagnetization

Depth (m)	Rock type	Sample Number	ALTERNATING FIELD (AF)		THERMAL (TG)	
			Inclination (°)	Intensity (mT)	Inclination (°)	Intensity (mT)
0.0	silty clay	HYA1	59.4	2.21	N	AF
1.0	silty clay	HYA2	53.5	1.20	N	AF
2.0	silty clay	HYA3	-73.7	2.12	R	AF
3.0	silty clay	HYA4	-5.0	0.29	R	AF
4.0	silty clay	HYA5	52.1	2.05	N	AF
5.0	silty clay	HYA6	58.5	1.52	N	AF
6.0	silty clay	HYA7	49.8	1.47	N	AF
7.0	silty clay	HYA8	59.8	0.81	N	AF
8.0	silty clay	HYA9	36.2	0.62	N	AF
9.0	silty clay	HYA10	3.2	2.28	N	AF
10.0	silty clay	HYA11	52.6	1.08	N	AF
11.0	silty clay	HYA12	72.1	0.97	N	AF
12.0	silty clay	HYA13	35.6	1.12	N	AF
14.0	silty clay	HYA14	66.7	2.76	N	AF
15.0	silty clay	HYA15	69.3	1.96	N	AF
16.0	silty clay	HYA16	60.4	2.48	N	AF
17.0	silty clay	HYA17	49.8	1.61	N	AF
18.0	silty clay	HYA18	45.8	1.39	N	AF
19.0	silty clay	HYA19	46.7	4.51	N	AF
20.0	silty clay	HYA20	21.5	1.57	N	AF
21.0	silty clay	HYA21	33.3	0.58	N	AF
22.0	silty clay	HYA22	46.8	1.32	N	AF
23.0	silty clay	HYA23	60.9	2.11	N	AF
24.0	silty clay	HYA24	16.1	3.10	N	AF
25.0	silty clay	HYA25	50.0	0.86	N	AF
26.0	silty clay	HYA26	50.7	0.54	N	AF
27.0	silty clay	HYA27	35.2	1.79	N	AF
28.0	silty clay	HYA28	42.8	0.44	N	AF
29.0	silty clay	HYA29	45.1	0.49	N	AF
30.0	silty clay	HYA30	40.4	1.48	N	AF
31.0	silty clay	HYA31	52.6	2.06	N	AF
32.0	silty clay	HYA32	45.0	0.78	N	AF
33.0	silty clay	HYA33	43.2	1.04	N	AF
34.0	silty clay	HYA34	60.2	1.12	N	AF
35.0	silty clay	HYA35	58.0	0.94	N	AF
36.0	silty clay	HYA36	33.1	1.32	N	AF
37.0	silty clay	HYA37	53.4	5.47	N	AF
38.0	silty clay	HYA38	60.1	0.48	N	AF
39.0	silty clay	HYA39	62.3	2.26	N	AF
40.0	silty clay	HYA40	40.4	1.18	N	AF
41.0	silty clay	HYA41	46.2	1.82	N	AF
42.0	silty clay	HYA42	65.2	0.98	N	AF
43.0	silty clay	HYA43	58.1	1.38	N	AF
44.0	silty clay	HYA44	31.2	0.92	N	AF
45.0	silty clay	HYA45	-64.1	1.71	R	AF

Supplemental Materials. Table S1: Inclination and polarity results for whole core from alternating field and thermal demagnetization. Table S2: Composite polarity stratigraphy. Please visit <https://doi.org/10.1130/GES01629.S1> or access the full-text article on [www.gsapubs.org](http://www.gsapubs.org) to view the Supplemental Materials.

we did not use the declination data because the core barrel was spun during recovery, rotating the core about a vertical axis relative to original depositional position. Core recovery was typically >90%, but reduced to ~40%–60% in coarser intervals. In the field, we split the core in half and then collected 2 cm cubic paleomagnetic specimens at intervals of 0.3–1 m, depending on the availability of a suitable lithology (mud to silt; Table S1<sup>1</sup>). Specimens were encapsulated in square boxes of non-magnetic plastic. We analyzed samples from the entire core length using alternating field (AF) demagnetization. All demagnetization steps and remanence measurements were made in magnetically shielded rooms (<300 nT). The upper 202 specimens were measured in the Paleomagnetism Laboratory of the Institute of Geology and Geophysics, Chinese Academy of Sciences (CAS), with the remaining samples from the

lower part of the core measured at the Institute of Tibetan Plateau Research, CAS. The samples were systematically demagnetized in 12–14 discrete steps at intervals of 5–10 mT, usually up to a maximum of 80–110 mT. At each step, the remanent intensities were measured using a 2G Enterprises 755 superconducting rock magnetometer. The dynamic range of the magnetometer is  $2.0 \times 10^{-12}$  to  $2.0 \times 10^{-4}$  A·m<sup>2</sup>, and the sensitivity is  $1.0 \times 10^{-12}$  A·m<sup>2</sup>.

In the lower part of the core, we collected a parallel set of samples for thermal demagnetization (TD). Samples were collected at intervals of 0.3–0.5 m, from a depth of ~180 m to the base of the sedimentary section. All TD measurements were made in the Paleomagnetism Laboratory at the University of California, Davis. Systematic thermal demagnetization of the natural remanent magnetization (NRM) was conducted using an ASC Scientific TD-48

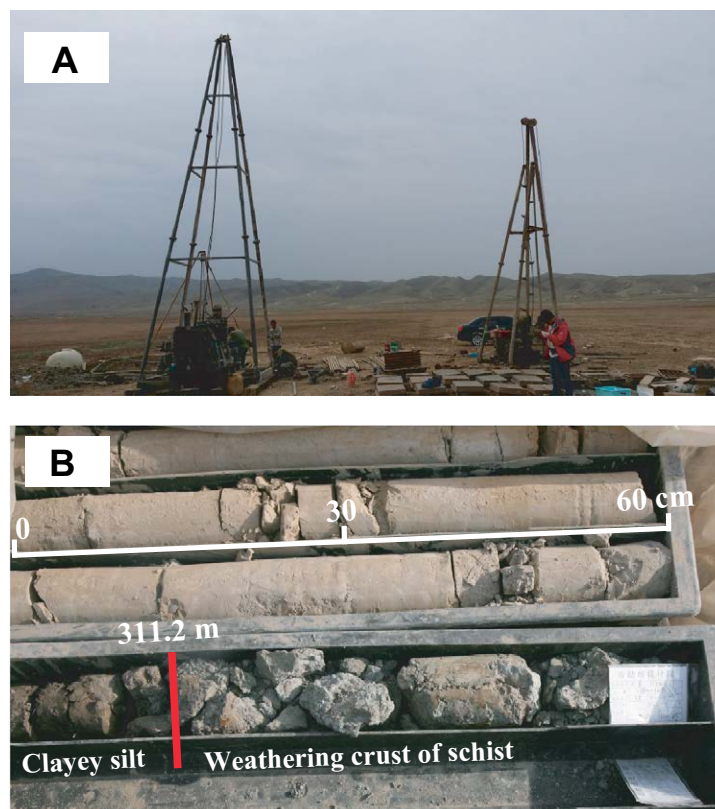


**Figure 3.** Photographs of the borehole HY-C8 drilling site (36.66465°N; 105.25591°E) viewed toward the northeast, with Huangjiawa range in the distance (A), and a core sample showing the contact at the base of the Ganyanchi Basin at a depth of ~311.2 m (B) (photograph taken after core had dried). Note the distinct lithological differences near the base, with blue weathering crust developed on pre-Cambrian schist below and brown clayey silt above.

thermal demagnetizer. Samples were stepwise heated in 20–60 °C increments to a maximum temperature of 690 °C (14 demagnetization steps). After each demagnetization step, the remanent intensities were measured on a 2G Enterprises 755 superconducting rock magnetometer housed in a magnetically shielded space (<300 nT). The dynamic range of the magnetometer is  $1.0 \times 10^{-12}$  to  $2.0 \times 10^{-4}$  A·m<sup>2</sup>, and the sensitivity is  $1.0 \times 10^{-12}$  A·m<sup>2</sup>. In addition, after each demagnetization step, the magnetic susceptibility was measured using a Bartington MS2 magnetic susceptibility meter.

Data for both AF and TD measurements were analyzed using Zplotit software (Acton, 2011), and sample directions were determined using principal component analysis (Kirschvink, 1980). Characteristic magnetization (ChRM) component directions were determined using stable components with at least

four, but typically five to nine, demagnetization steps trending toward the origin. The origin was included as a point by a forced-to-origin step. Analyses were not included in our final magnetostratigraphic analysis if the samples were incompletely demagnetized, ChRM directions could not be determined due to ambiguous direction or intensity in the demagnetization diagrams, or the maximum angular deviation (MAD) of the ChRM was >20°.

We determined SAR by correlating the magnetic polarity zonation observed in the core with the geomagnetic polarity time scale (GPTS; Hilgen et al., 2012; Singer, 2014), and then dividing the thickness of the polarity zones observed in the core by their duration in the GPTS. To calculate incremental SAR values, we divided the thickness of each interval by its duration, where thickness (duration) was determined by subtracting the depth to (age of the) overlying boundary from the depth to (age of) the boundary. We did not decompact the core because of the short length (328 m) and predominance of loose sediment that is not lithified.

## RESULTS

### Core Stratigraphy

The core can be divided into six major lithological units (Table 1). The contact between unit 1 (weathered muscovite schist) and unit 2 (massive muddy silt) at 311.2 m depth is sharp and separates units with distinctly different lithologies (Fig. 3B). Therefore, we assign the depth of 311.2 m as the base of the sedimentary fill in the Ganyanchi pull-apart basin at the site of the core. Analysis of the stratigraphy indicates that the whole core profile is dominated by fine-grained deposits (~97%), such as silty clay or clayey silt, except for unit 4, which is an 11.2-m-long section of gravel; however, the matrix of unit 4 is also fine-grained. We found no evidence of a significant hiatus in the profile, based on the absence of abrupt and significant changes in sediment type or grain size and the lack of evidence of obvious erosional surfaces such as paleosols or lag conglomerates. Based on the fine-grained nature of the deposits and the position of the core close to the active depocenter, we infer that the Ganyanchi Basin probably has been continuously accumulating sediments since its initial formation.

### Paleomagnetic Measurements

Table S1 (footnote 1) indicates sample numbers and inclination and MAD values for the AF and TD analyses, and Figure 4 shows representative demagnetization plots.

### Alternating Field Demagnetization

A total of 397 samples were collected for AF demagnetization, of which 373 yielded results (Table S1), although 33 of these samples had demagnetization behavior that was difficult to interpret. We take an endpoint at 100 mT during

TABLE 1. LITHOSTRATIGRAPHY OF GANYANCHI BASIN CORE HY-C8, NORTHEASTERN TIBET

Unit	Depth (m)		Thickness (m)	Description
	Top	Bottom		
6	0	240	240	Grey to dark-gray silty clay interbedded with light blueish silt, displaying 0.5–3-cm-thick horizontal lamination. This unit contains numerous peat horizons that are typically 3 to 25 cm thick and particularly numerous below 80 m depth. The dark color of the silt is likely due to elevated concentrations of organic material.
5	240	283	43	Brick-red, well-sorted, massive clayey silt, with minor fine gravel intervals containing clasts that are typically <5 mm in diameter.
4	283	294.2	11.2	Dominated by ~0.3–0.5-m-thick layers of gray, matrix-supported gravel, interlayered with a number of well-sorted, laminated, brick-red silt horizons. The matrix of the gravel comprises fine sand and silt. Clasts in the gravel are poorly rounded or angular, 2–4 cm in diameter, and mainly pre-Cambrian muscovite schist, with rare Oligocene sandstone.
3	294.2	302.3	8.1	Brick-red, silty clay. The middle of the unit comprises a 2.6-m-thick interval of gray-brown silt.
2	302.3	311.2	8.9	Massive, gray to gray-brown muddy silt.
1	311.2	328	>16.8	Weathering crust of the late Proterozoic bedrock (muscovite schist). Crystalline basement flooring the basin. Bottom not exposed. We correlate the schist with late Proterozoic bedrock units exposed in the flanking ranges, based on lithologic similarity (Fig. 2B).

the fit of the AF demagnetization data. The intensity of the NRM for these samples was on the order of  $10^{-4}$  to  $10^{-6}$  A/m. Representative AF demagnetization diagrams are presented in Figure 4. Most samples (86%) showed good demagnetization behavior, while 57 samples (14%) were rejected using the criteria mentioned in the Methods section. Overall, we recovered ChRM directions for 340 samples (i.e.,  $397 - 57 = 340$ ). Based on their demagnetization behaviors, the 340 samples can be classified into two categories. (1) One group exhibits nearly linear decay to the origin (Figs. 4A–4C), indicative of a stable ChRM direction. A total of 247 samples show this behavior. (2) The other group shows a clear change of remanent direction at 25–30 mT (Fig. 4E), indicating the removal of a secondary remanent magnetization. Above 25–30 mT, the remanent directions decay to the origin and a ChRM can be easily isolated. This type of sample is common below 260 m in the core (54 samples).

### Thermal Demagnetization

We obtained TD results from a total of 182 samples at depths between 180 m and the base of the core (Table S1 [footnote 1]). The intensity of the NRM for these samples was on the order of  $10^{-4}$  to  $10^{-7}$  A/m. Representative TD demagnetization diagrams are presented in Figures 4G–4H. After removal of a low-temperature secondary overprint at 150–200 °C (Fig. 4G), 150 samples (~82%) unblocked at ~580 °C, with 11 samples (~6%) unblocking at ~690 °C (Fig. 4G). This demagnetization behavior may indicate that magnetite and hematite are the principal ChRM carriers in the Ganyanchi Basin. In general, the ChRM is represented by a relatively straightforward unidirectional trajectory toward the origin of orthogonal vector demagnetization plots from 200 to 580 °C (Figs. 4G–4H). Data from at least four (but typically seven to ten) consecutive demagnetization steps above 200 °C were used to determine the ChRM direction, with a MAD of  $<10^\circ$  (but typically  $<5^\circ$ ) for the respective line fits (Table S1 [footnote 1]).

Some of the TD samples had magnetic susceptibilities that increased by one or even two orders of magnitude, starting at ~400 °C. However, such samples did not show large increases in magnetic remanence, indicating that the new magnetic phases did not acquire a strong remanent magnetization. To further evaluate the remanence increases, we compared fits to the TD data up to, and including, both 400 and 600 °C. For almost all TD analyses, including the samples with large increases in magnetic susceptibility, data fit to 400 °C yielded best-fit inclinations that were within a few degrees of those obtained using all of the data fit to 600 °C. In three cases, the polarities differed between the two fits because the inclinations were nearly horizontal. The agreement between the two sets of analyses is further evidence that the increases in magnetic susceptibility at high temperature did not compromise the magnetic remanence. The best-fit inclinations reported in Table S1 (footnote 1) are fits to 600 °C.

### Magnetostratigraphy and Correlation to the GPTS

The two sets of magnetic polarity data for the lower part of the core allowed us to build a composite magnetic polarity zonation. A total of 166 samples have both AF and TD results. Of these, the AF and TD polarities agree in 120 samples (~72%), in which case we used the TD data in the composite polarity zonation, due to greater confidence in achieving complete demagnetization. For the remaining cases, where polarities determined from the AF and TD analyses disagree, we systematically reviewed the data for both analyses and classified the results as either high or low quality (*Q*). *Q* is a subjective assessment that is based on objective criteria such as the scatter in the demagnetization data, the progressive decrease in intensity during demagnetization, and in the case of TD, changes in the magnetic susceptibility (or lack thereof). Results with low *Q* could be due to development of iron sulfide (melnikovite or pyrrhotite) as a magnetic carrier (Fig. 4I) or the presence of a very hard magnetic component in some samples (Fig. 4J).

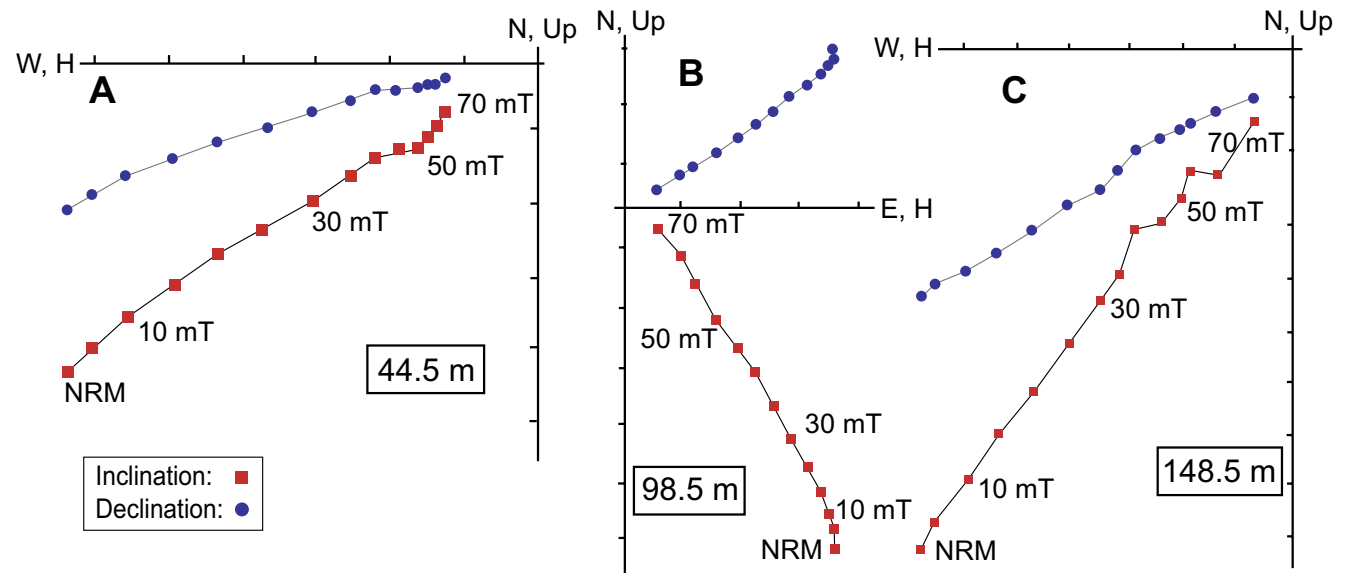
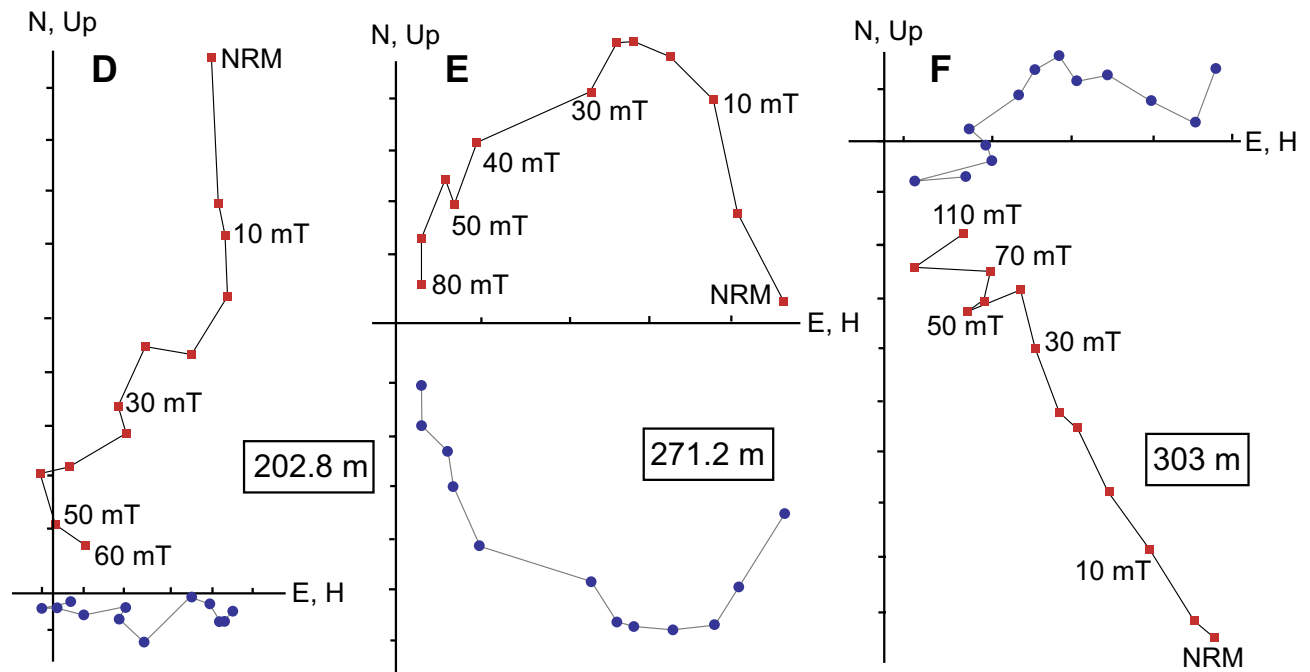


Figure 4 (on this and following two pages). Representative demagnetization diagrams for samples (identified by core depth) from the Ganyanchi pull-apart basin. NRM—natural remanent magnetization. (A–F) Alternating field demagnetization.





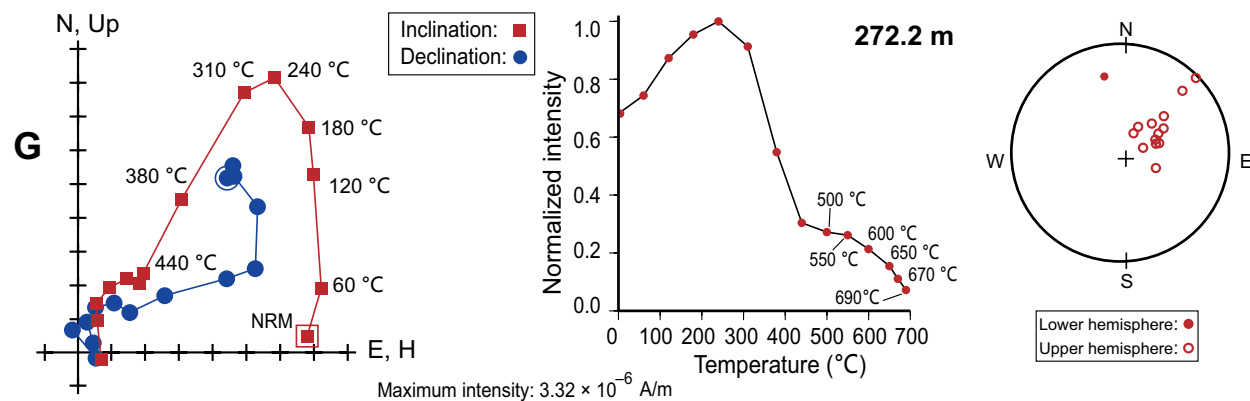
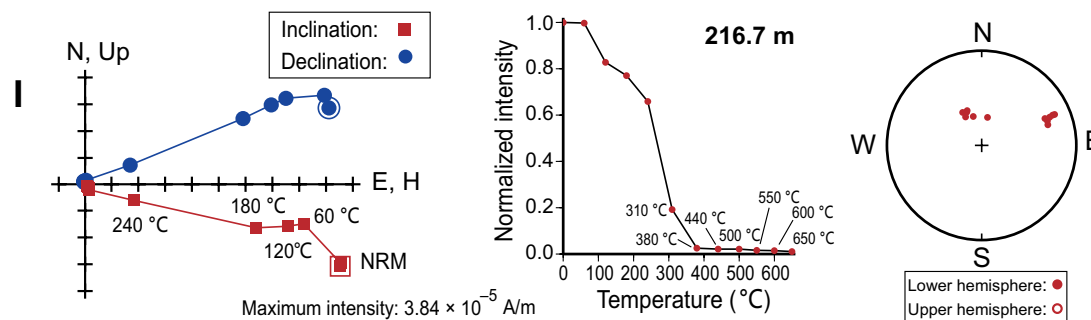
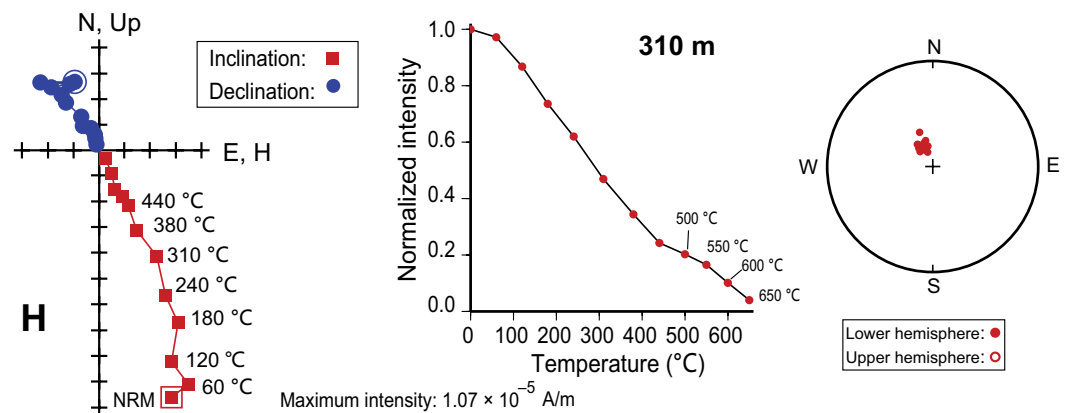
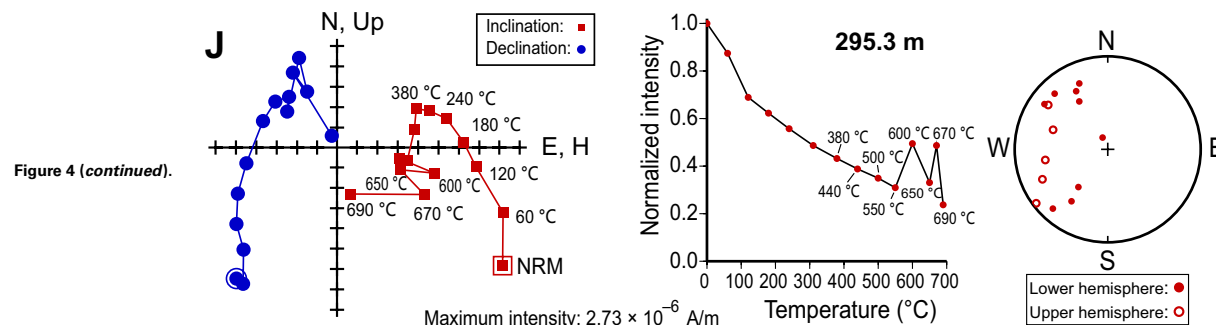


Figure 4 (continued). (G–J) Thermal demagnetization. H—horizontal projection. Normalized intensity is normalized to the maximum of each sample. Some samples show evidence of melnikovite or pyrrhotite (panel I, the intensity, middle column, decreases significantly between 240 °C–380 °C and to a very low level) or a very hard magnetic component (panel J, about 20–30% of the intensity is left even when the temperatures reach up to 690 °C).





We applied this quality analysis to a total of 49 samples, 46 for which AF and TD polarities disagreed when the TD data were fit to 600 °C, plus an additional three for which AF and TD polarities did not match when the TD data were fit to 400 °C; all samples compared are indicated in Table S1 (footnote 1). AF results had higher *Q* than TD for 19 of these cases, while 11 had the opposite case. We discarded 15 samples with low *Q* in both AF and TD, plus three samples with high *Q* for both AF and TD that we were unable to reconcile.

In total we identified 25 polarity intervals (13 normal, 12 reversed) in the Ganyanchi core, which are marked as N1–N13 and R1–R12 in Figures 5 and 6. We defined polarity epochs only when at least two successive specimens displayed the same polarity and thus exclude epochs that would be based on only a single specimen. In the upper 180 m of the core, there are six such single-sample polarity zones, as indicated by small open circles in Figure 5. These may represent noise or six geomagnetic excursions in the Brunhes normal polarity chron. However, we did not investigate this young signal further because it is not the focus of the present study, which is on dating the base of the core.

The Ganyanchi Basin is located in a region of western China that lacks significant late Cenozoic volcanism. As a result, there are no dateable ashes within the section to provide ties to the GPTS. Likewise, the restricted nature of the basin sediments precludes lithostratigraphic correlations to other sections with biostratigraphic age control, such as within the Sikouzi basin (see Fig. 1, blue diamond labeled as “1”) (Wang et al., 2011). However, radiocarbon dating from paleoseismic trenching studies (see location in Fig. 2B) indicate that the age of the very top ground surface in Ganyanchi Basin is effectively zero (i.e., dates of 150 yr at depth of ~0.4 m) (Liu-Zheng et al., 2015). Therefore, we assume the top of the core is zero age, consistent with its normal polarity and position in an active basin.

The complexity of the magnetic zonation in the lower portion of the core, together with the lack of independent age constraints within the core, precludes a definitive correlation between the observed magnetic polarity zonation and the GPTS. To address this problem, we consider two possible correlations, a young model that uses the GPTS for the last 2.8 m.y. (Singer, 2014) and an old model that correlates with the last 5 m.y. of the GPTS (Hilgen et al., 2012). Both

models assume zero age at the top of the core, no hiatuses in deposition, and a simple direct correlation of polarity zones with known chrons or subchrons in the reference GPTS. The SAR values implied by each model are shown in Figure 7 and listed in Tables 2 and 3. Note that the SAR values shown in Figure 7 differ from the incremental values in Tables 2 and 3 because they are averaged over multiple increments.

In the young model (Fig. 6), we correlate the three relatively long normal polarity intervals (N1, N7, and N13) with the Brunhes, Olduvai, and Gauss normal polarity chrons and the intermediate-length intervals (N2, N3, and N10) with the Jaramillo, Cobb Mountain, and Reunion subchrons in the Matuyama reversed polarity chron, respectively. There remain several short normal polarity intervals that do not appear to correlate with the GPTS. Although these intervals could reflect localized remagnetization, there are several very short subchrons or geomagnetic excursions in the Matuyama that have been reported in various marine cores (e.g., Singer, 2014) and from elsewhere in northeastern Tibet (Zhang et al., 2012; Song et al., 2005). If we include these in the GPTS, the observed polarity intervals correlate fairly well with the GPTS (see left side of Fig. 6). Using this correlation, the whole section can be estimated to have formed between the Gauss normal polarity chron and the present day. This correlation gives a minimum age for the base of the core as well as the smallest difference between the sedimentation rate for the top and bottom halves of the core (Fig. 7; Table 2).

We also construct an old model (Fig. 6), in which we correlate the two long normal polarity intervals N1 and N7 with chrons C1n and C2An.1n (Hilgen et al., 2012), respectively. In this correlation, we interpret the upper long normal polarity zone (N1) to represent the Brunhes normal polarity chron, and the reversed polarity intervals R1–R6 to correspond to the Matuyama reverse polarity chron, with intervals N5 and N6 representing the Olduvai and Reunion normal polarity subchrons within the Matuyama. Below interval N7, this model correlates interval N13 with chron C3n.4n, in which case the base of the core would be no older than ca. 5.23 Ma (Hilgen et al., 2012). This correlation yields a large change in average sedimentation rate between the bottom and top halves of the core (Fig. 7; Table 3).

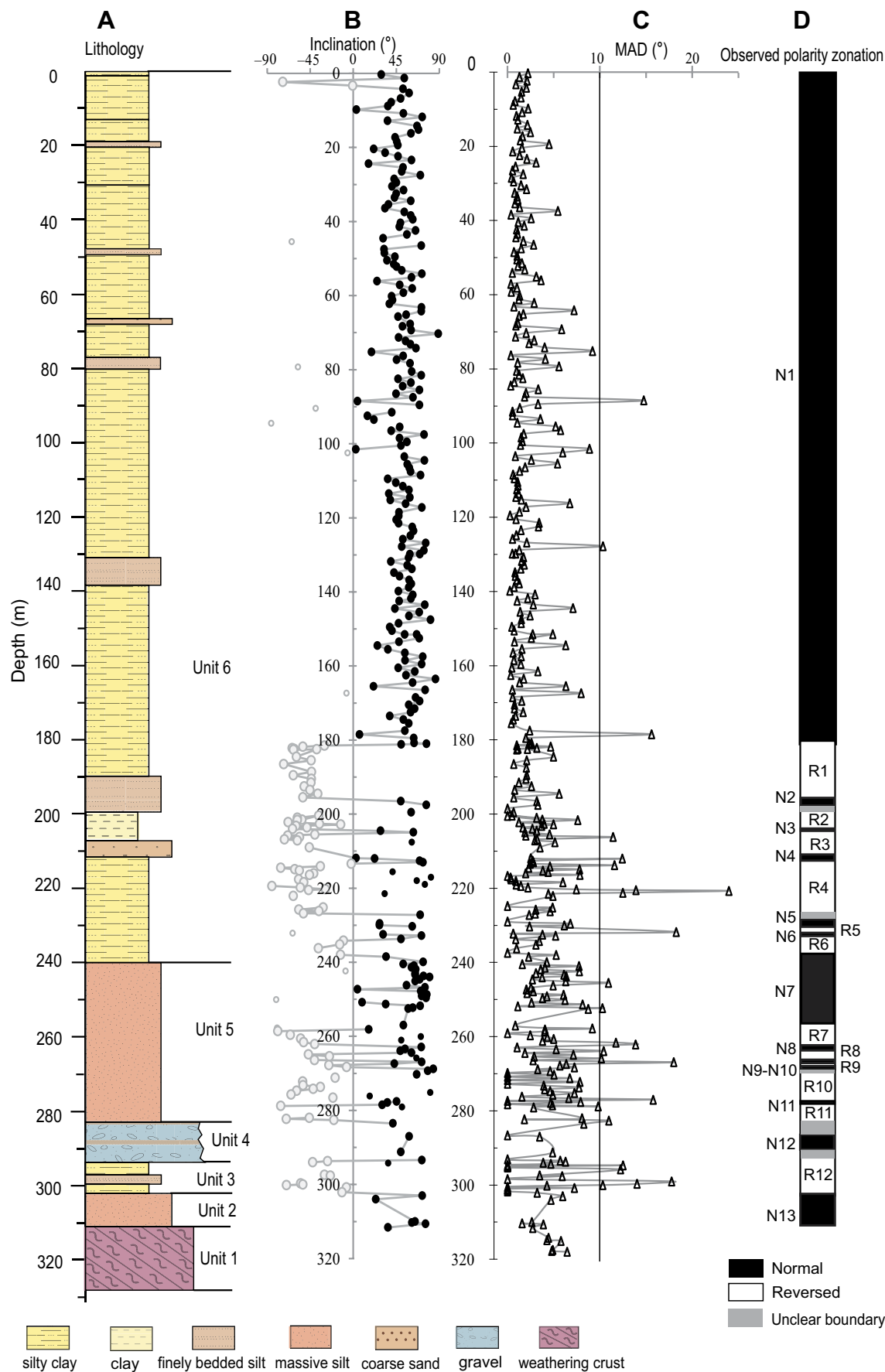


Figure 5. Stratigraphy of the Ganyanchi Basin core plotted as depth below modern surface. Vertical scales are the same in all plots. (A) Lithology; see legend at the base of the figure for rock types. (B) Composite magnetic inclination; see Table S2 (footnote 1) for data. Filled and open circles represent positive and negative inclinations, respectively. Small symbols not connected by tie lines represent single samples within zones of opposite polarity of polarity opposite that of adjacent samples. (C) Maximum angular deviation (MAD) of the characteristic remanent magnetization. (D) Polarity zonation (N, normal; R, reversed). Gray bands indicate uncertainty in boundary positions between normal and reversed polarity chrons.

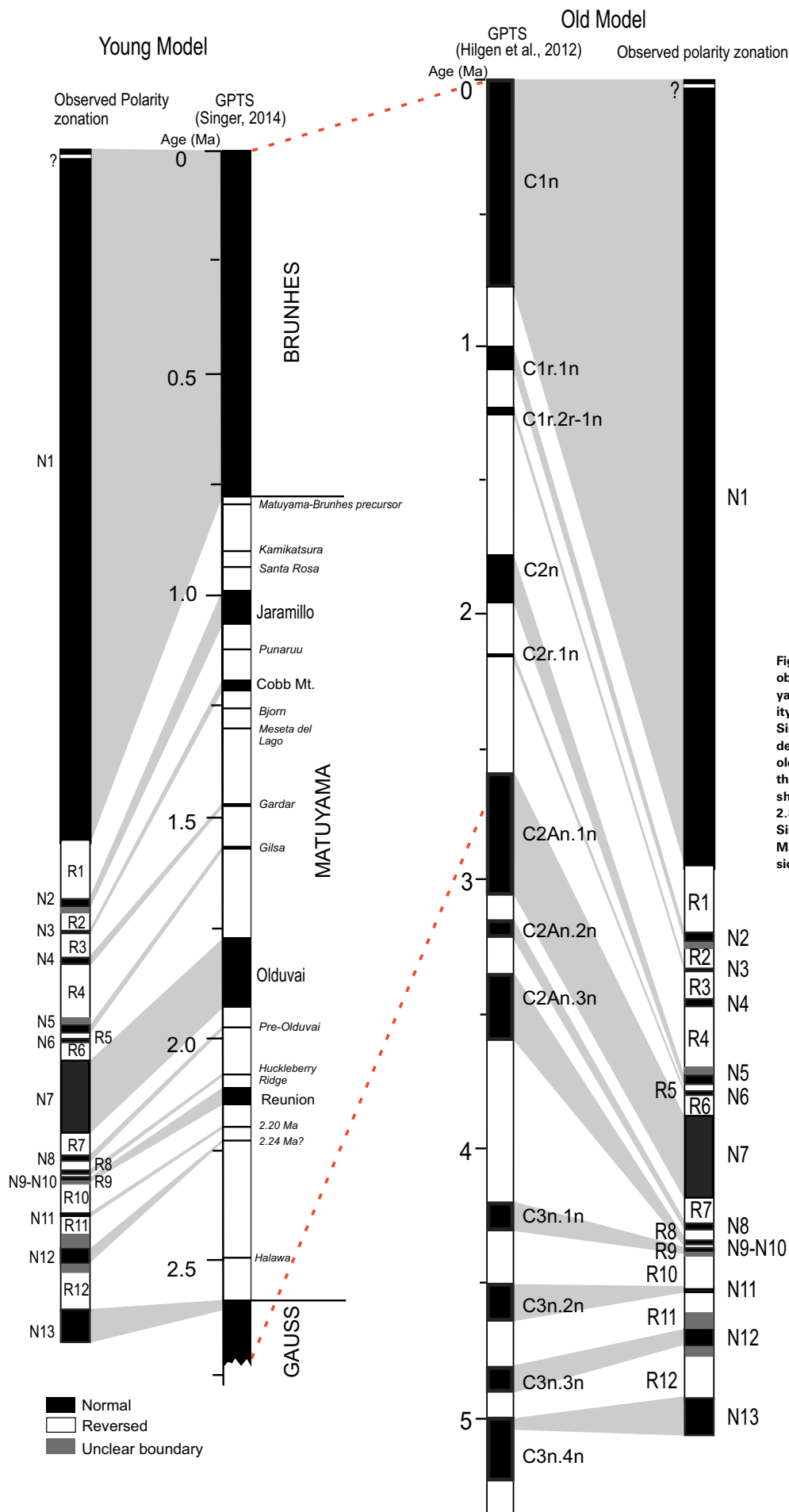


Figure 6. End-member correlations of the observed magnetostratigraphy of the Gan-yanchi Basin to the geomagnetic polarity time scale (GPTS; Hilgen et al., 2012; Singer, 2014); see Tables 2 and 3 for age-depth correlations. Right half shows the old model (ca. 5 m.y.) correlations with the GPTS of Hilgen et al. (2012). Left half shows the enlarged young model (ca. 2.8 m.y.) correlating with the GPTS of Singer (2014); italicized names within the Matuyama epoch represent short excursions. See text for explanation.

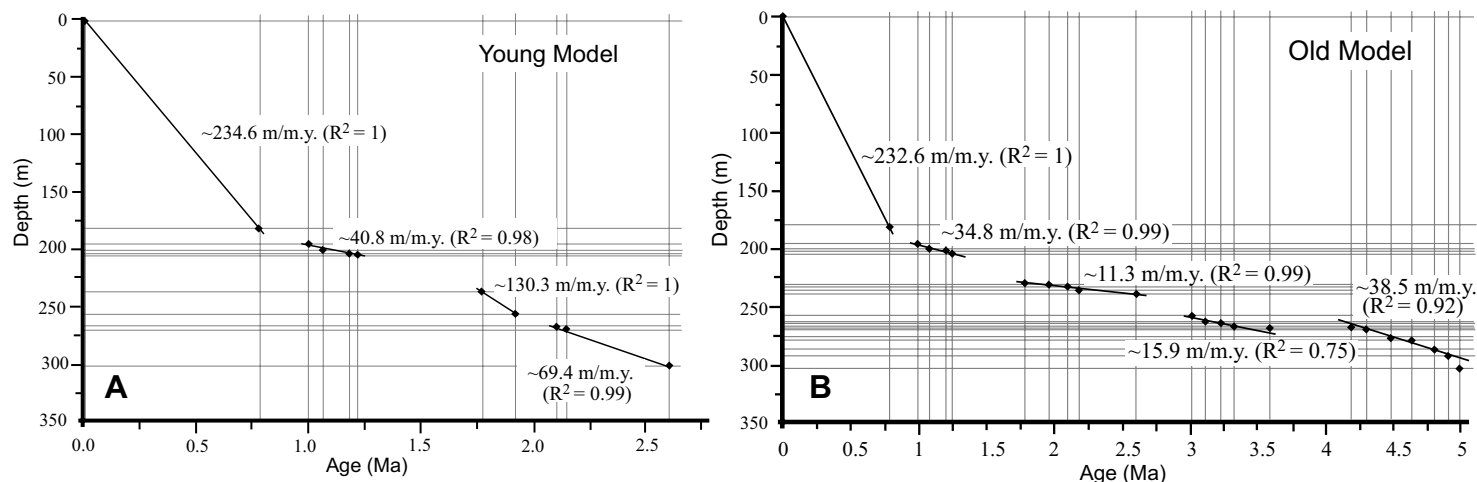


Figure 7. Plots of stratigraphic depth versus magnetostratigraphic age in the Ganyanchi Basin core for the end-member young (A) and old (B) age models shown in Figure 6 and reported in Tables 2 and 3. Horizontal and vertical lines indicate ages and corresponding depths from Tables 2 and 3, for young and old models, respectively. Linear fits indicate sediment accumulation rates (SARs) averaged over multiple intervals. Note that in the deeper part of the core (>200 m), SARs are generally significantly lower in the old model than in the young model. R<sup>2</sup> values indicate the goodness of fit for the linear regressions.

In the young model, there are seven excursions in the GPTS scale that have no correlative magnetozone in the Ganyanchi magnetic polarity stratigraphy, as indicated in the left side of Figure 6 (i.e., M-B Matuyama-Brunhes precursor, Kamikatsura, Santa Rosa, Punaruu, Bjorn, Meseta del Lago, and Halawa). Several explanations are possible for the absence of these excursions in the Ganyanchi core, including the existence of brief depositional hiatuses during these short-lived magnetic events, the possibility that our sampling missed

these excursions, or the possibility that samples from these short, normal polarity intervals were later overprinted with reversed polarity. Additionally, there is one short normal polarity chron (N6) in the young model and one (N4) in the old model (Fig. 6) that have no correlative chrons on the GPTS. These non-correlatable magnetochrons may be unrecognized cryptochrons within the GPTS, or they may be attributable to local remagnetization or errors introduced during sampling or laboratory analysis (e.g., Lease et al., 2012).

TABLE 2. YOUNG AGE MODEL AND IMPLIED SEDIMENTATION RATES FOR GANYANCHI CORE

Depth* (m)	Age <sup>†</sup> (Ma)	Sedimentation rate <sup>§</sup> (m/m.y.)	Geomagnetic polarity time scale (Singer, 2014)
181.35 ± 0.15	0.773	234.6	Brunhes-Matuyama boundary
196.0 ± 0.50	1.001	64.3	Jaramillo (top)
200.0 ± 0.50	1.069	58.8	Jaramillo (bottom)
204.25 ± 0.25	1.189	35.4	Cobb Mountain (top)
205.20 ± 0.30	1.221	29.7	Cobb Mountain (bottom)
238.25 ± 0.25	1.775	59.7	Olduvai (top)
257.4 ± 0.40	1.922	130.3	Olduvai (bottom)
268.55 ± 0.25	2.115	57.8	Reunion (top)
270.55 ± 0.25	2.155	50.0	Reunion (bottom)
302.55 ± 0.45	2.61	70.3	Gauss (top)

\*Depth is the mean of the samples above and below the magnetic boundary. Error is one-half the distance between the two samples.

<sup>†</sup>Uncertainties on the age of chron boundaries not reported in the source publication.

<sup>§</sup>Rate corresponds to that for the interval immediately above this horizon.

TABLE 3. OLD AGE MODEL AND IMPLIED SEDIMENTATION RATES FOR GANYANCHI CORE

Depth* (m)	Age <sup>†</sup> (Ma)	Sedimentation rate <sup>§</sup> (m/m.y.)	Geomagnetic polarity time scale (Hilgen et al., 2012)
181.35 ± 0.15	0.781	232.2	C1n (start)
196.00 ± 0.50	0.988	70.8	C1r.1n (end)
200.00 ± 0.50	1.072	47.6	C1r.1n (start)
204.25 ± 0.25	1.220	28.7	C1r.2r-1n (end)
205.20 ± 0.30	1.240	47.5	C1r.2r-1n (start)
229.25 ± 0.25	1.778	44.7	C2n (end)
231.05 ± 0.75	1.945	10.8	C2n (start)
232.35 ± 0.15	2.115	7.6	C2r.1n (end)
233.95 ± 0.25	2.153	42.1	C2r.1n (start)
238.25 ± 0.25	2.581	10.0	C2An.1n (end)
257.40 ± 0.40	3.032	42.5	C2An.1n (start)
262.50 ± 0.40	3.116	60.7	C2An.2n (end)
264.65 ± 0.25	3.207	23.6	C2An.2n (start)
266.65 ± 0.25	3.330	16.3	C2An.3n (end)
267.60 ± 0.20	3.596	3.6	C2An.3n (start)
268.55 ± 0.25	4.187	1.6	C3n.1n (end)
270.55 ± 0.25	4.300	17.7	C3n.1n (start)
277.45 ± 0.15	4.493	35.8	C3n.2n (end)
278.05 ± 0.15	4.631	4.3	C3n.2n (start)
286.80 ± 0.20	4.799	52.1	C3n.3n (end)
292.15 ± 0.95	4.896	55.2	C3n.3n (start)
302.55 ± 0.45	4.997	103.0	C3n.4n (end)

\*Depth is the mean of the samples above and below the magnetic boundary. Error is one-half the distance between the two samples.

<sup>†</sup>Uncertainties on the age of chron boundaries not reported in the source publication.

<sup>§</sup>Rate corresponds to that for the interval immediately above this horizon.

Finally, we emphasize that the magnetic polarity stratigraphy is based on analysis of inclination only, because the declination data cannot be used due to the likelihood of vertical-axis rotation of the core during removal. Such an analysis may produce a different polarity than one based on virtual geomagnetic poles (VGP). It might well be that some of the short chrons or excursions that appear in the Ganyanchi magnetic polarity stratigraphy are the result of using only the inclination data. However, the presence of these short chrons or excursions does not change the overarching magnetostratigraphic correlation or our final interpretation regarding overall trends in sediment accumulation rate or the age of the basin.

## DISCUSSION

### Sedimentation Rates in the Ganyanchi Basin

In both the young and old models, deposition rates in the upper part of the core are higher than those in the lower part, although the difference is greatest for the old model (Fig. 7; Tables 2 and 3). The young model shows two significant pulses of elevated SAR, one between ca. 1.92 and ca. 1.78 Ma,

when the rate was 130.3 m/m.y., and a second after 0.77 Ma, when the rate was 234.6 m/m.y. (Fig. 7A). The average SAR along the entire core is ~115.9 m/m.y. In contrast, the mean SAR in the old model is very slow for most of the record (i.e., <40 m/m.y. from ca. 5 to ca. 1 Ma) (Fig. 7B), increasing to ~234.6 m/m.y. from 0.77 Ma to present. The SAR values for the top portion of the core are the same in both models because in both, the long normal polarity interval N1 is correlated with the Brunhes normal polarity chron (Fig. 6).

It is useful to compare the SAR values we report here for the Ganyanchi Basin with those from magnetostratigraphic studies of other terrestrial basins in the northern Tibetan Plateau region (Table 4), the locations of which are shown in Figure 1 as blue diamonds. Elevated SAR values during the Brunhes epoch are also observed in the western Qaidam (Zhang et al., 2012) and the Kunlun Shan Pass (Song et al., 2005) basins. However, the slow SARs in the lower part of the core implied by the old model are anomalous for this region during this time period. For example, mean SAR values (Table 4) are >128 m/m.y. in the Sikouzi Basin during 4.5–0.5 Ma (Wang et al., 2011), ~158.5 m/m.y. in Lanzhou basin during ca. 2.2–0.78 Ma (Zhang et al., 2016), ~81 m/m.y. in Xining basin during ca. 2–0.78 Ma (Lu et al., 2012), >200 m/m.y. in the Guide Basin during 7.0–1.8 Ma (Fang et al., 2005), >260 m/m.y. during ca. 6.5–1.8 Ma in the eastern Qaidam Basin (Fang et al., 2007), >170 m/m.y. during the span of 3.58–1.07 Ma

TABLE 4. SEDIMENT ACCUMULATION RATES (SARs) DURING OLD (7 TO 0.78 Ma) AND YOUNG (&lt;ca. 1 Ma TO PRESENT) TIME INTERVALS IN NORTHEASTERN TIBET

Basin (core) name	Latitude (°N)	Longitude (°E)	Old time interval (Ma)	Mean SAR, old interval (m/m.y.)*	Lithology, old interval	Young time interval (Ma)	Mean SAR, young interval (m/m.y.)*	Lithology, young interval	Reference
Ganyanchi (HY-C8)	36.66	105.26	ca. 2.7–0.8	~69.4–130.3	Sediment	0.78–0	~234.6	Sediment	This study
Sikouzi	36.15	106.10	4.5–0.5	>128	Rock	n.d.	n.d.	n.d.	Wang et al., 2011
Lanzhou (Xijin)	36.02	103.75	ca. 2.2–0.78	~158.5 <sup>†</sup>	Loess	0.78–0	~245 <sup>†</sup>	Loess	Zhang et al., 2016
Xining (PZS)	36.65	101.84	ca. 2–0.78	~81 <sup>†</sup>	Loess	0.78–0	~112 <sup>†</sup>	Loess	Lu et al., 2012
Xining (DDL)	36.66	101.79	n.d.	n.d.	n.d.	ca. 1.07–0	~129	Loess	Lu et al., 2012
Guide	36.10	101.45	7.0–1.8	>200	Rock	n.d.	n.d.	n.d.	Fang et al., 2005
Eastern Qaidam	37.25	96.7	6.5–1.8	>260	Rock	n.d.	n.d.	n.d.	Fang et al., 2007
Kunlun Shan Pass	35.49	93.37	3.58–1.07	>170	Rock	ca. 1.07–0.5	>600	Rock	Song et al., 2005
Western Qaidam (15YZK01)	37.97	93.2	1.95–0.78	>262	Sediment	0.78–0	460	Sediment	Chen et al., 2017
Western Qaidam (SG-1)	38.41	92.51	2.58–0.78	>261	Rock	0.78–0.1	~438	Sediment and rock	Zhang et al., 2012
Western Qaidam (SG-1b)	38.35	92.27	2.58–1.6	~90	Sediment and rock	n.d.	n.d.	n.d.	Zhang et al., 2014
Eastern Tarim (Ls2)	39.49	88.18	7.07–1.77 1.77–0.78	~185 ~38 <sup>†</sup>	Sediment and rock sediment	0.78–0	~47 <sup>†</sup>	Sediment	Chang et al., 2012

Note: n.d.—no data.

\*Reported without correcting for post-depositional compaction. Rates from rock are thus minima.

<sup>†</sup>SAR not reported in the original publication; calculated from reported data.

in the Kunlun Shan Pass Basin (Song et al., 2005), and ~185 m/m.y. during 7.07–1.77 Ma in the eastern Tarim Basin (Chang et al., 2012). Three studies from the western Qaidam Basin yield rates of >262 m/m.y. during the interval ca. 1.95–0.78 Ma (core 15YZK01; Chen et al., 2017), >261 m/m.y. in the interval 2.58–0.78 Ma (core SG-1; Zhang et al., 2012), and ~90 m/m.y. during 2.58–1.6 Ma (core SG-1b; Zhang et al., 2014). The young model yields higher SARs for the lower portion of the core (69.4–130.3 m/m.y.) that are closer to the values reported from these other basins.

It is worth noting that although the SARs from other basins in the northern Tibetan Plateau region can provide a general reference for those expected in the Ganyanchi Basin, we expect SAR to vary significantly across the region due to differences in the specific depositional environments and settings of each basin, including local climatic and/or tectonic controls. For example, SAR values from the western Qaidam Basin were likely affected by deformation in active fold-thrust belts or by left-lateral slip along the Altyn Tagh fault (Zhang et al., 2012), whereas SAR in the Tarim Basin was influenced not only by surface uplift of the Tibetan Plateau but also local aridification (Chang et al., 2012). In addition, we note that the SAR values from the Ganyanchi Basin are derived from un lithified sediments, whereas a number of the SAR values from the other basins are derived from rock thicknesses that have not been corrected for compaction, and thus are expected to be lower than the true accumulation rates. However, such minimum SAR values provide a reference for reasonable SAR values expected from the Ganyanchi Basin. Based on this reference, we choose the young model as the preferred one because the SAR values are unreasonably slow in the old model.

Loess provenance studies based on U-Pb zircon ages indicate that the Qaidam Basin and adjacent regions were probable dust sources for the Chinese Loess Plateau (Fig. 1) during Quaternary glacial periods (Pullen et al., 2011), when westerly winds carried millions of tons of dust from the northern Tibetan Plateau region to the Loess Plateau to the northeast. The Ganyanchi Basin lies along the dust-storm tracks between the Qaidam Basin to the west and the Chinese Loess Plateau to the east, and extensive dust deposits accumulated in and around the basin (Fig. 2). Thus, erosional and depositional records from the Qaidam region and the Loess Plateau, respectively, may provide insights on the depositional history of the Ganyanchi Basin. Kapp et al. (2011) suggested that the erosion rates due to westerly winds in the Qaidam Basin were >120–1100 m/m.y. during the last 2.8 m.y. Using astronomically tuned ages, SAR values for the central Chinese Loess Plateau have been >60 m/m.y. since 2.6 Ma (Han et al., 2011). Thus, the wind erosional records indicate that the SAR values we find here are reasonable, with values for the Ganyanchi Basin of 130–235 m/m.y., with an average of ~116 m/m.y., falling between the rates in the Qaidam Basin and the Loess Plateau.

### Age of the Ganyanchi Basin

To constrain the age of the base of the sedimentary section, we combine sedimentation rates from the lower part of the core with the thickness of sediment between the lowest observed reversal (N13-R12) and the contact between units 1 and 2. The N13-R12 reversal occurs in the interval 302.1–303.0 m

(Table S2 [footnote 1]), and the base of the sedimentary section is at 311.2 m, indicating the core samples 8.2–9.1 m of sediment between the N13-R12 boundary and the base of the core. In the young model, the N13-R12 reversal corresponds to the Gauss-Matuyama boundary at 2.610 Ma (Singer, 2014). Figure 7 indicates an average SAR of  $\sim 130.3$  m/m.y. for the three lowest dated intervals in the core. In detail, SAR values for the first two intervals above the Gauss-Matuyama boundary are 70.3 m/m.y. and 50.0 m/m.y. (Table 2), indicating an extrapolated age for the base of the section of  $2.76 \pm 0.03$  Ma.

In the old model, the N13-R12 reversal corresponds to the end of chron C3n.4n at 4.997 Ma, and SARs for the first two overlying intervals are 103.0 and 55.2 m/m.y. (Table 3), indicating an extrapolated age for the base of the section of  $5.12 \pm 0.04$  Ma. As noted above, we prefer the young age model because (1) it provides sedimentation rates more similar to those in surrounding basins, (2) it correlates better to the GPTS, and (3) high SAR values are expected for the active tectonic environment of the Ganyanchi pull-apart basin. Thus, we conclude that the Ganyanchi Basin had started forming by  $2.76 \pm 0.03$  Ma. Exploring the tectonic implications of this age is beyond the scope of the present study because doing so requires a detailed review of prior work on the timing of deformation in northeastern Tibet and along the Haiyuan fault system, as well as the use of seismic data to first establish both the structural context of the core and the relationship between the basin deposits and slip on the basin-bounding faults. We address these topics in a on the basin-bounding faults, we will address these topics in a separate study.

### Implications for Northeastern Tibet

The SARs allow us to explore the depositional history of the Haiyuan region. As noted above, the young model indicates increased SARs in two intervals, from ca. 1.92 to 1.78 Ma and from 0.77 Ma to present. We interpret these two periods to reflect accelerated sediment transport and deposition in the Ganyanchi Basin due to the combined effects of late Cenozoic Northern Hemisphere cooling and tectonic activity within the Haiyuan fault system. The Northern Hemisphere entered into a period of rapid cooling during the late Miocene and early Pliocene (Zachos et al., 2001) that continued through the whole Quaternary (Shackleton et al., 1990; Zachos et al., 2001). We interpret the pulses of accelerated SAR to result from enhanced erosion and sediment transport in the region of the Ganyanchi Basin resulting from frequent and abrupt changes in temperature, precipitation, and vegetation during the late Cenozoic (e.g., Zhang et al., 2001). A nearly 1000-m-deep core collected in the western Qaidam Basin (at  $\sim 38.4^\circ\text{N}$ ,  $92.5^\circ\text{E}$ ; Fig. 1, blue diamond labeled with “9”) (Zhang et al., 2012) shows broadly similar patterns of sedimentation as reported here for the Ganyanchi Basin, suggesting that regional climate change has played an important role in modulating the pacing of sedimentary infilling of basins in the northeastern Tibetan Plateau since late Pliocene time. Moreover, an overall trend toward a drier and cooler climate since ca. 2.8 Ma is indicated by multiple records (Fig. 8), including broadleaf pollen content in the

western Qaidam Basin (Cai et al., 2012), eolian dust mass accumulation rates on the central Chinese Loess Plateau (Sun and An, 2005), sea-surface temperatures from the North Atlantic Ocean at Ocean Drilling Program Site 982 (Lawrence et al., 2009), and stacked benthic  $\delta^{18}\text{O}$  records (Lisiecki and Raymo, 2005) (Fig. 8). The correlation of changes in the Ganyanchi SAR record with changes in the climate-proxy records shown in Figure 8 supports the inference of strong climatic control on the sedimentation in Ganyanchi Basin and the northeastern Tibetan Plateau, indicating that SAR values have increased as the regional climate has shifted toward overall drier and cooler conditions. Comparison of SAR values across the northeastern Tibetan Plateau (Table 4; Fig. 1) indicates a general trend toward higher SAR values for the times after ca. 1 Ma, with lower SAR values at earlier times, consistent with our inference that climate exerted an important control on sedimentation patterns in the broad region of northeastern Tibet.

Tectonic movement also likely contributed to the increase in SAR that started at ca. 1.9 Ma, considering that the Ganyanchi Basin formed within the Haiyuan fault zone. Specifically, extension along the basin-bounding master faults likely uplifted the surrounding mountains relative to the basin floor, leading to a local “bathtub” basin-filling process such as has been inferred for larger basins within the interior of the Tibetan Plateau (e.g., Tapponnier et al., 2001; Zhang et al., 2017). In a controversial interpretation, it appears that the northern Tibetan Plateau experienced a significant episode of surface uplift in middle to late Miocene time (e.g., Molnar, 2005; Zheng et al., 2006; Wang et al., 2016), the amplitude of which is estimated to be  $\sim 1$ – $2$  km (Molnar, 2005). After this uplift phase, deformation in the region appears to have switched to large-scale strike-slip movement. Because the Ganyanchi Basin is a pull-apart basin along the Haiyuan fault, we infer that onset of deposition by 2.76 Ma implies that the bounding fault system had similarly formed by this time, and that deformation in the Haiyuan area had thus shifted to left-lateral slip by at least this time. A ca. 2.76 Ma onset of Haiyuan faulting in the Ganyanchi Basin area predates the age suggested by Burchfiel et al. (1991), but is generally consistent with the timing for the transition to strike-slip deformation observed elsewhere along the northeastern margin of the Tibetan Plateau (e.g., Duvall et al., 2013). In a separate study, we investigate both the link between the onset of sedimentation within the Ganyanchi Basin and formation of the Haiyuan fault, and the transition to strike-slip–dominated deformation in the northeastern Tibetan Plateau.

It is likely that the effect of bathtub basin-filling in the Haiyuan area may be less intense than elsewhere in the region, due to both the lower elevation of the surrounding ranges and the lower topographic relief between them and the basin floor. Elevations in high-relief mountain ranges such as the Qilian Shan or Kunlun Shan exceed 4000 m, and such ranges stand as much as 2000 m above the adjacent basins whereas the adjacent intermountain basins they flank are less than 2800 m in elevation. In contrast, the Ganyanchi Basin is at  $\sim 2000$  m elevation, with only  $\sim 500$ – $800$  m of relief between the basin floor and surrounding ranges. Because of the lower absolute elevations and relief, we expect that the intensity of alpine glaciation and associated sediment transport was lower in the Ganyanchi area than in the high-altitude, high-relief



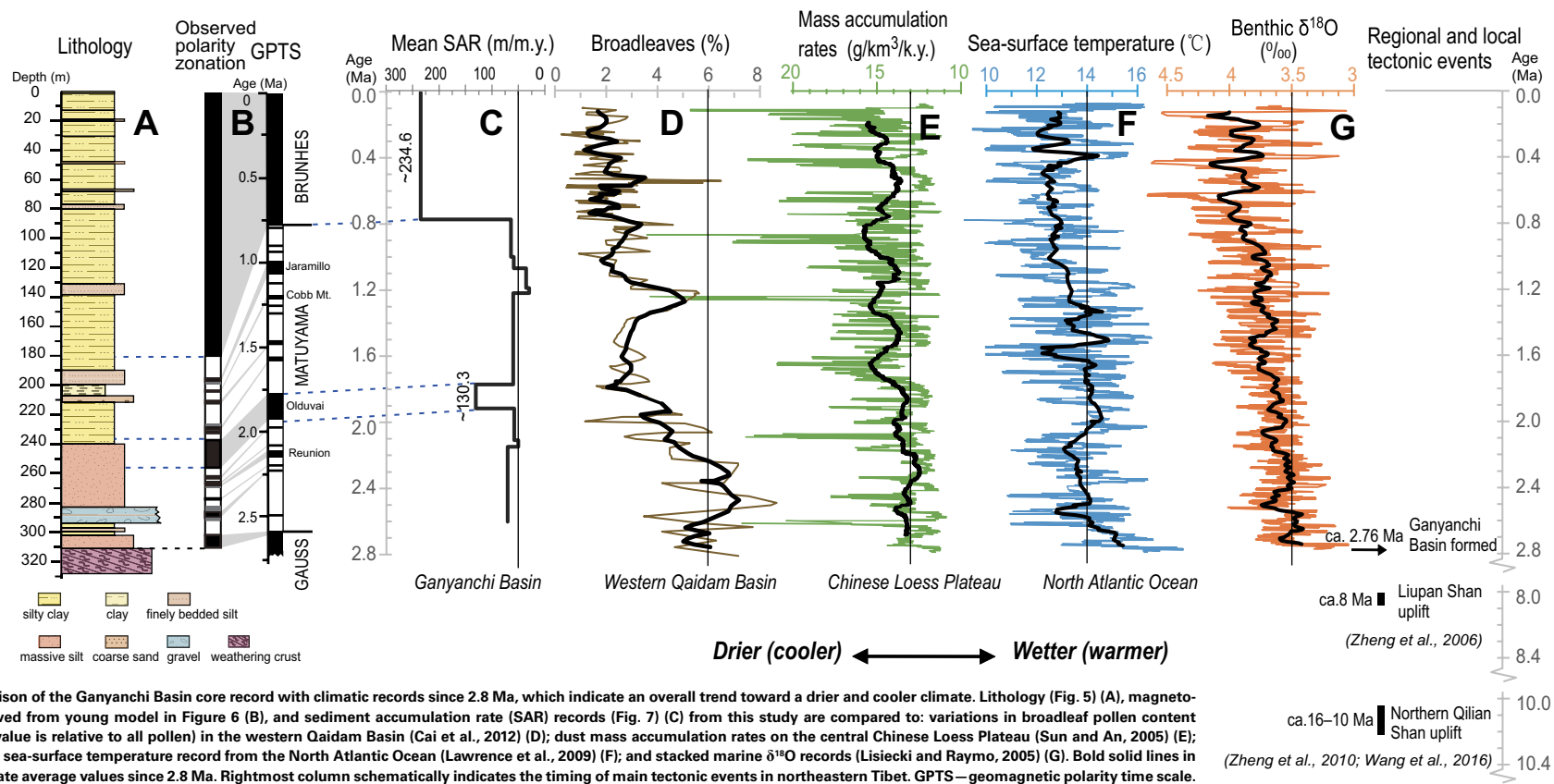


**Figure 8.** Comparison of the Ganyanchi Basin core record with climatic records since 2.8 Ma, which indicate an overall trend toward a drier and cooler climate. Lithology (Fig. 5) (A), magnetostratigraphy derived from young model in Figure 6 (B), and sediment accumulation rate (SAR) records (Fig. 7) (C) from this study are compared to: variations in broadleaf pollen content (the percentage value is relative to all pollen) in the western Qaidam Basin (Cai et al., 2012) (D); dust mass accumulation rates on the central Chinese Loess Plateau (Sun and An, 2005) (E); alkenone-derived sea-surface temperature record from the North Atlantic Ocean (Lawrence et al., 2009) (F); and stacked marine  $\delta^{18}\text{O}$  records (Lisiecki and Raymo, 2005) (G). Bold solid lines in each record indicate average values since 2.8 Ma. Rightmost column schematically indicates the timing of main tectonic events in northeastern Tibet. GPTS—geomagnetic polarity time scale. (Zheng et al., 2006; Zheng et al., 2010; Wang et al., 2016)

basins farther into the interior of the Tibetan Plateau. Thus, we propose that the main role of the tectonic movement in the Haiyuan region was to provide accommodation by continuous left-normal oblique slip along the master faults bounding the pull-apart basin. Collectively, this probably suggests that climate change, rather than tectonic activity, was the major factor driving changes in depositional rates in the Haiyuan area.

### CONCLUSIONS

We present the first magnetostratigraphic investigation of the Ganyanchi (Salt Lake) Basin, which is the largest pull-apart basin along the active, left-lateral Haiyuan fault. The sample drill core reached bedrock flooring the basin at 311.2 m depth below the modern depositional surface. Using both alternating field and thermal demagnetizations, we identified 13 polarity zones within

the core using an inclination-only analysis due to the potential for vertical-axis rotation of the core during removal. Because we lack independent age control for the section (other than that the top of the core is of zero age), we present two end-member age models for correlating the observed polarity zonations with the geomagnetic polarity time scale. Based on the implied sedimentation rates, the low degree of induration of the deposits, and the tectonic setting of Ganyanchi pull-apart basin, we argue that the young model provides the best fit. In this model, the Ganyanchi Basin formed at ca.  $2.76 \pm 0.03$  Ma. This age implies that the flanking portions of the left-lateral Haiyuan fault had formed by at least ca. 2.8 Ma. The young age model indicates two phases of increased sediment accumulation rate in the basin, with one from ca. 1.92 to 1.78 Ma and the second from 0.77 Ma to present. We attribute these periods of enhanced deposition to Northern Hemisphere cooling and frequent climate change during the late Cenozoic, and suggest that the role of tectonics was primarily to create the accommodation needed to capture this depositional record.

## ACKNOWLEDGMENTS

This study was supported jointly by the National Science Foundation of China (grant 41272214) and the China Scholarship Council (201504190011). Science Editor Shanaka de Silva, Associate Editor Roberto Molina-Garza, and reviewers Peter Lippert and Josep Parés provided constructive, insightful comments that improved this manuscript. We greatly acknowledge Peng Zhang, Dawen Zhang, and Millie Levin for providing valuable suggestions during paleomagnetic analysis. We also thank our driver, Shixiang Li, for the great help provided during the field work.

## REFERENCES CITED

- Acton, G., 2011, ZPLOTIT software (version 2011-01): <http://paleomag.ucdavis.edu/software-zplotit.html>.
- An, Z.S., Kutzbach, J.E., Prell, W.L., and Porter, S.C., 2001, Evolution of Asian monsoons and phased uplift of the Himalaya–Tibetan Plateau since late Miocene time: *Nature*, v. 411, p. 62–66, <https://doi.org/10.1038/35075035>.
- Aydin, A., and Nur, A., 1982, Evolution of pull-apart basins and their scale independence: *Tectonics*, v. 1, p. 91–105, <https://doi.org/10.1029/TC0011001p00091>.
- Basile, C., and Brun, J.P., 1999, Transtensional faulting patterns ranging from pull-apart basins to transform continental margins: An experimental investigation: *Journal of Structural Geology*, v. 21, p. 23–37, [https://doi.org/10.1016/S0191-8141\(98\)00094-7](https://doi.org/10.1016/S0191-8141(98)00094-7).
- Burchfiel, B.C., Zhang, P., Wang, Y., Zhang, W., Song, F., Deng, Q., Molnar, P., and Royden, L., 1991, Geology of the Haiyuan fault zone, Ningxia Hui Autonomous Region, China, and its relation to the evolution of the northeastern margin of the Tibetan Plateau: *Tectonics*, v. 10, p. 1091–1110, <https://doi.org/10.1029/90TC02685>.
- Cai, M., Fang, X., Wu, F., Miao, Y., and Appel, E., 2012, Pliocene–Pleistocene stepwise drying of Central Asia: Evidence from paleomagnetism and sporopollen record of the deep borehole SG-3 in the western Qaidam Basin, NE Tibetan Plateau: *Global and Planetary Change*, v. 94–95, p. 72–81, <https://doi.org/10.1016/j.gloplacha.2012.07.002>.
- Chang, H., An, Z.S., Liu, W.G., Qiang, X.K., Song, Y.G., and Ao, H., 2012, Magnetostratigraphic and paleoenvironmental records for a Late Cenozoic sedimentary sequence drilled from Lop Nor in the eastern Tarim Basin: *Global and Planetary Change*, v. 80–81, p. 113–122, <https://doi.org/10.1016/j.gloplacha.2011.09.008>.
- Chen, A., Zheng, M., Shi, L., Wang, H., and Xu, J., 2017, Magnetostratigraphy of deep drilling core 15YZK01 in the northwestern Qaidam Basin (NE Tibetan Plateau): Tectonic movement, salt deposits and their link to quaternary glaciation: *Quaternary International*, v. 436, p. 201–211, <https://doi.org/10.1016/j.quaint.2017.01.026>.
- Clark, M.K., Farley, K.A., Zheng, D., Wang, Z.C., and Duvall, A.R., 2010, Early Cenozoic faulting on the northern Tibetan Plateau margin from apatite (U–Th)/He ages: *Earth and Planetary Science Letters*, v. 296, p. 78–88, <https://doi.org/10.1016/j.epsl.2010.04.051>.
- Deng, Q., Song, F., Zhu, S., Li, M., Wang, T., Zhang, W., Burchfiel, B.C., Molnar, P., and Zhang, P., 1984, Active faulting and tectonics of the Ningxia-Hui Autonomous Region, China: *Journal of Geophysical Research*, v. 89, p. 4427–4445, <https://doi.org/10.1029/JB089iB06p04427>.
- Deng, Q., Zhang, W., Zhang, P., Jiao, D., Song, F.M., Wang, Y., Burchfiel, B.C., Molnar, P., Royden, L., Chen, S., Zhu, S., and Chai, C., 1989, Haiyuan strike-slip fault zone and its compressional structures at the end: Dizhen Dizhi, v. 11, p. 1–14 (in Chinese with English abstract).
- Ding, G.Y., Chen, J., Tian, Q.J., Shen, X.H., Xing, C.Q., and Wei, K.B., 2004, Active faults and magnitudes of left-lateral displacement along the northern margin of the Tibetan Plateau: *Tectonophysics*, v. 380, p. 243–260, <https://doi.org/10.1016/j.tecto.2003.09.022>.
- Dupont-Nivet, G., Krijgsman, W., Langereis, C.G., Abels, H.A., Dai, S., and Fang, X.M., 2007, Tibetan plateau aridification linked to global cooling at the Eocene–Oligocene transition: *Nature*, v. 445, p. 635–638, <https://doi.org/10.1038/nature05516>.
- Duvall, A.R., Clark, M.K., Kirby, E., Farley, K.A., Craddock, W.H., Li, C.Y., and Yuan, D.-Y., 2013, Low-temperature thermochronometry along the Kunlun and Haiyuan Faults, NE Tibetan Plateau: Evidence for kinematic change during late-stage orogenesis: *Tectonics*, v. 32, p. 1190–1211, <https://doi.org/10.1002/tect.20072>.
- Fang, X.M., Yan, M.D., Van der Voo, R., Rea, D.K., Song, C., Parés, J.M., Gao, J.P., Nie, J.S., and Dai, S., 2005, Late Cenozoic deformation and uplift of the NE Tibetan Plateau: Evidence from high-resolution magnetostratigraphy of the Guide Basin, Qinghai Province, China: *Geological Society of America Bulletin*, v. 117, p. 1208–1225, <https://doi.org/10.1130/B257271>.
- Fang, X.M., Zhang, W.L., Meng, Q.Q., Gao, J.P., Wang, X.M., King, J., Song, C.H., Dai, S., and Miao, Y.F., 2007, High-resolution magnetostratigraphy of the Neogene Huaitoutala section in the eastern Qaidam Basin on the NE Tibetan Plateau, Qinghai Province, China and its implication on tectonic uplift of the NE Tibetan Plateau: *Earth and Planetary Science Letters*, v. 258, p. 293–306, <https://doi.org/10.1016/j.epsl.2007.03.042>.
- Guo, Z.T., Ruddiman, W.F., Hao, Q.Z., Wu, H.B., Qiao, Y.S., Zhu, R.X., Peng, S.Z., Wei, J.J., Yuan, B.Y., and Liu, T.S., 2002, Onset of Asian desertification by 22 Myr ago inferred from loess deposits in China: *Nature*, v. 416, p. 159–163, <https://doi.org/10.1038/416159a>.
- Han, W., Fang, X., Berger, A., and Yin, Q., 2011, An astronomically tuned 8.1 Ma eolian record from the Chinese Loess Plateau and its implication on the evolution of Asian monsoon: *Journal of Geophysical Research*, v. 116, D24114, <https://doi.org/10.1029/2011JD016237>.
- Hilgen, F.J., Lourens, L.J., and van Dam, J.A., 2012, The Neogene period, in Gradstein, F.M., Ogg, J.G., Schmitz, M., and Ogg, G., eds., *The Geologic Time Scale 2012*: Amsterdam, Elsevier, p. 923–985.
- Institute of Geology, China Earthquake Administration (IGCEA), and Seismological Bureau of Ningxia Hui Autonomous Region (SBNHAG), 1990, The Haiyuan active fault zone: Beijing, Seismological Press (in Chinese with English brief introduction), p. 6–120.
- Institute of Seismology, Lanzhou, State Seismological Bureau (ISL), and Seismological Bureau of Ningxia Hui Autonomous Region (SBNHAG), 1980, The great Haiyuan earthquake in 1920: Beijing, Seismological Press (in Chinese with English brief introduction), p. 10–34.
- Kapp, P., Pelletier, J.D., Rohrmann, A., Heermance, R., Russell, J., and Ding, L., 2011, Wind erosion in the Qaidam basin, central Asia: Implications for tectonics, paleoclimate, and the source of the Loess Plateau: *GSA Today*, v. 21, p. 4–10, <https://doi.org/10.1130/GSATG99A.1>.
- Kirschvink, J.L., 1980, The least-squares method line and plane and analysis of paleomagnetic data: *Geophysical Journal International*, v. 62, p. 699–718, <https://doi.org/10.1111/j.1365-246X.1980.tb02601.x>.
- Lawrence, K.T., Herbert, T.D., Brown, C.M., Raymo, M.E., and Haywood, A.M., 2009, High-amplitude variations in North Atlantic sea surface temperature during the early Pliocene warm period: *Paleoceanography*, v. 24, PA2218, <https://doi.org/10.1029/2008PA001669>.
- Lease, R.O., Burbank, D.W., Hough, B., Wang, Z., and Yuan, D., 2012, Pulsed Miocene range growth in northeastern Tibet: Insights from Xunhua Basin magnetostratigraphy and provenance: *Geological Society of America Bulletin*, v. 124, p. 657–677, <https://doi.org/10.1130/B30524.1>.
- Li, C.Y., Zhang, P.-z., Yin, J.H., and Min, W., 2009, Late Quaternary left-lateral slip rate of the Haiyuan fault, northeastern margin of the Tibetan Plateau: *Tectonics*, v. 28, p. 357–369, <https://doi.org/10.1029/2008TC002302>.
- Li, Y.B., Ran, Y.K., Wang, H., and Wu, F.Y., 2014, Paleoseismic records of large earthquakes on the cross-basin fault in the Ganyanchi pull-apart basin, Haiyuan fault, northeastern Tibetan Plateau: *Natural Hazards*, v. 71, p. 1695–1713, <https://doi.org/10.1007/s11069-013-0983-5>.
- Lisiecki, L.E., and Raymo, M.E., 2005, A Pliocene–Pleistocene stack of 57 globally distributed benthic  $\delta^{18}\text{O}$  records: *Paleoceanography*, v. 20, PA1003, <https://doi.org/10.1029/2004PA001071>.
- Liu-Zeng, J., Shao, Y.X., Klinger, Y., Xie, K., Yuan, D.Y., and Lei, Z.S., 2015, Variability in magnitude of paleoearthquakes revealed by trenching and historical records, along the Haiyuan Fault, China: *Journal of Geophysical Research: Solid Earth*, v. 120, p. 8304–8333, <https://doi.org/10.1002/2015JB012163>.
- Lu, H.Y., Wang, X., Wang, X., Sun, X.F., Yi, S.W., Zhou, Y.L., Liu, Q.Y., Swinehart, J., and Vandenberghe, J., 2012, Palaeoclimatic changes in northeastern Qinghai-Tibetan Plateau revealed by magnetostratigraphy and magnetic susceptibility analysis of thick loess deposits: *Netherlands Journal of Geoscience*, v. 91, no. 1–2, p. 189–198, <https://doi.org/10.1017/S001677460000158X>.
- Mann, P., Hempton, M.R., Bradley, D.C., and Burke, K., 1983, Development of pull-apart basins: *The Journal of Geology*, v. 91, p. 529–554, <https://doi.org/10.1086/628803>.
- Molnar, P., 2005, Mio-Pliocene growth of the Tibetan Plateau and evolution of east Asian climate: *Paleontologia Electronica*, v. 8, 8.1.2, 23 p.
- Ningxia Bureau of Geology and Mineral Resources (NBGM), 1989, *Regional Geology of Ningxia Hui Autonomous Region*: Beijing, Geological Publishing House, p. 194–196 (in Chinese with English brief introduction).
- Pares, J.M., Van der Voo, R., Downs, W.R., Yan, M.D., and Fang, X.M., 2003, Northeastward growth and uplift of the Tibetan Plateau: Magnetostratigraphic insights from the Guide Basin: *Journal of Geophysical Research*, v. 108, <https://doi.org/10.1029/2001JB001349> (erratum available at <https://doi.org/10.1029/2003JB002624>).

- Pullen, A., Kapp, P., McCallister, A.T., Chang, H., Gehrels, G.E., Garzione, C.N., Heermance, R.V., and Ding, L., 2011, Qaidam Basin and northern Tibetan Plateau as dust sources for the Chinese Loess Plateau and paleoclimatic implications: *Geology*, v. 39, p. 1031–1034, <https://doi.org/10.1130/G32296.1>.
- Shackleton, N.J., Berger, A., and Peltier, W.R., 1990, An alternative astronomical calibration of the lower Pleistocene timescale based on ODP Site 677: *Transactions of the Royal Society of Edinburgh: Earth Sciences*, v. 81, p. 251–261, <https://doi.org/10.1017/S0263593300020782>.
- Singer, B.S., 2014, A quaternary geomagnetic instability time scale: *Quaternary Geochronology*, v. 21, p. 29–52, <https://doi.org/10.1016/j.quageo.2013.10.003>.
- Song, C.H., Gao, D.L., Fang, X.M., Cui, Z.J., Li, J.J., Yang, S.L., Jin, H.B., Burbank, D., and Kirschvink, J.L., 2005, High-resolution magnetostratigraphy of late Cenozoic sediments from the Kunlun Shan Pass Basin and its implications on deformation and uplift of the northern Tibetan Plateau: *Chinese Science Bulletin*, v. 50, p. 1912–1922, <https://doi.org/10.1360/03wd0314>.
- Sun, Y.B., and An, Z.S., 2005, Late Pliocene–Pleistocene changes in mass accumulation rates of eolian deposits on the central Chinese Loess Plateau: *Journal of Geophysical Research*, v. 110, D23101, <https://doi.org/10.1029/2005JD006064>.
- Tapponnier, P., Xu, Z., Roger, F., Meyer, B., Arnaud, N., Wittlinger, G., and Yang, J., 2001, Oblique stepwise rise and growth of the Tibet Plateau: *Science*, v. 294, p. 1671–1677, <https://doi.org/10.1126/science.105978>.
- Wang, W.T., Zhang, P.Z., Kirby, E., Wang, L.H., Zhang, G.L., Zheng, D.W., and Chai, C.Z., 2011, A revised chronology for Tertiary sedimentation in the Sikouzi basin: Implications for the tectonic evolution of the northeastern corner of the Tibetan Plateau: *Tectonophysics*, v. 505, p. 100–114, <https://doi.org/10.1016/j.tecto.2011.04.006>.
- Wang, W.T., Zhang, P.Z., Yu, J.X., Wang, Y.Z., Zheng, D.W., Zheng, W.J., Zhang, H.P., and Pang, J.Z., 2016, Constraints on mountain building in the northeastern Tibet: Detrital zircon records from synorogenic deposits in the Yumen Basin: *Scientific Reports*, v. 6, <https://doi.org/10.1038/srep27604>.
- Yuan, D.Y., Ge, W.P., Chen, Z.W., Li, C.Y., Wang, Z., Zhang, H., Zhang, P., Zheng, D., Zheng, W., Craddock, W.H., Dayem, K.E., Duvall, A.R., Hough, B., Lease, R.O., Champagnac, J., Burbank, D.W., Clark, M.K., Farley, K.A., Garzione, C.N., Kirby, E., Molnar, P., and Roe, G.H., 2013, The growth of northeastern Tibetan and its relevance to large-scale continental geodynamics: A review of recent studies: *Tectonics*, v. 32, p. 1358–1370, <https://doi.org/10.1002/tect.20081>.
- Zachos, J., Pagani, M., Sloan, L., Thomas, E., and Billups, K., 2001, Trends, rhythms, and aberrations in global climate 65 Ma to present: *Science*, v. 292, p. 686–693, <https://doi.org/10.1126/science.1059412>.
- Zhang, H.P., Zhang, P.Z., Prush, V., Zheng, D.W., Zheng, W.J., Wang, W.T., Liu, C.C., and Ren, Z.K., 2017, Tectonic geomorphology of the Qilian Shan in the northeastern Tibetan Plateau: Insights into the plateau formation processes: *Tectonophysics*, v. 707, p. 103–115, <https://doi.org/10.1016/j.tecto.2017.04.016>.
- Zhang, J., Li, J., Guo, B., Ma, Z., Li, X., Ye, X., Yu, H., Liu, J., Yang, C., Zhang, S., Song, C., Hui, Z., and Peng, T., 2016, Magnetostratigraphic age and monsoonal evolution recorded by the thickest Quaternary loess deposit of the Lanzhou region, western Chinese Loess Plateau: *Quaternary Science Reviews*, v. 139, p. 17–29, <https://doi.org/10.1016/j.quascirev.2016.02.025>.
- Zhang, P., Burchfiel, B.C., Molnar, P., Zhang, W., Jiao, D., Deng, Q., Wang, Y., Royden, L., and Song, F., 1991, Amount and style of late Cenozoic deformation in the Liupan Shan area, Ningxia Autonomous Region, China: *Tectonics*, v. 10, p. 1111–1129, <https://doi.org/10.1029/90TC02686>.
- Zhang, P.Z., Molnar, P., and Downs, W.R., 2001, Increased sedimentation rates and grain sizes 2–4 Myr ago due to the influence of climate change on erosion rates: *Nature*, v. 410, p. 891–897, <https://doi.org/10.1038/35073504>.
- Zhang, W.L., Appel, E., Fang, X.M., Song, C.H., and Cirpka, O., 2012, Magnetostratigraphy of deep drilling core SG-1 in the western Qaidam Basin (NE Tibetan Plateau) and its tectonic implications: *Quaternary Research*, v. 78, p. 139–148, <https://doi.org/10.1016/j.yqres.2012.03.011>.
- Zhang, W.L., Appel, E., Fang, X., Song, C., Setzer, F., Herb, C., and Yan, M.D., 2014, Magnetostratigraphy of drill-core SG-1b in the western Qaidam Basin (NE Tibetan Plateau) and tectonic implications: *Geophysical Journal International*, v. 197, p. 90–118, <https://doi.org/10.1093/gji/ggt439>.
- Zheng, D., Zhang, P.-Z., Wan, J., Yuan, D., Li, C., Yin, G., Zhang, G., Wang, Z., Min, W., and Chen, J., 2006, Rapid exhumation at ~8 Ma on the Liupan Shan thrust fault from apatite fission-track thermochronology: Implications for growth of the northeastern Tibetan Plateau margin: *Earth and Planetary Science Letters*, v. 248, p. 198–208, <https://doi.org/10.1016/j.epsl.2006.05.023>.
- Zheng, D., Clark, M.K., Zhang, P., Zheng, W., and Farley, K.A., 2010, Erosion, fault initiation and topographic growth of the north Qilian Shan (northern Tibetan Plateau): *Geosphere*, v. 6, p. 937–941, <https://doi.org/10.1130/GES00523.1>.